Monthly Notices
of the
ROYAL ASTRONOMICAL SOCIETY

MNRAS **428,** 2389–2406 (2013) doi:10.1093/mnras/sts204

Molecular gas in the centre of nearby galaxies from VLT/SINFONI integral field spectroscopy – I. Morphology and mass inventory⋆

X. Mazzalay,[1†] R. P. Saglia,[1,2] Peter Erwin,[1] M. H. Fabricius,[1,2] S. P. Rusli,[1,2] J. Thomas,[1,2] R. Bender,[1,2] M. Opitsch,[1] N. Nowak[3] and Michael J. Williams[1]

[1]*Max-Planck-Institut für extraterrestrische Physik, Postfach 1312, D-85741 Garching, Germany*
[2]*Universitätssternwarte, Scheinerstrasse 1, D-81679 München, Germany*
[3]*Max-Planck-Institut für Physik, Föhringer Ring 6, D-80805 München, Germany*

Accepted 2012 October 12. Received 2012 October 4; in original form 2012 August 10

ABSTRACT

We present the first results of an analysis of the properties of the molecular gas in the nuclear regions ($r \lesssim 300$ pc) of a sample of six nearby galaxies, based on new high-spatial-resolution observations obtained in the *K*-band with the near-infrared integral field spectrograph SINFONI at the Very Large Telescope. We derive 2D distributions of the warm molecular and ionized gas from the H_2, Brγ and He I emission lines present in the spectra of the galaxies. We find a range of morphologies, including bar- and ring-like distributions and either centrally peaked or off-centre emission. The morphologies of the molecular and the ionized gas are not necessarily coincident. The observed emission-line ratios point towards thermal processes as the principal mechanism responsible for the H_2 excitation in the nuclear and circumnuclear regions of the galaxies, independently of the presence of an active nucleus. We find that a rescaling of the H_2 2.12 μm emission-line luminosity by a factor $\beta \simeq 1200$ gives a good estimate (within a factor of 2) of the total (cold) molecular gas mass. The galaxies of the sample contain large quantities of molecular gas in their centres, with total masses in the $\sim 10^5$–10^8 $M_\odot$ range. Nevertheless, these masses correspond to less than 3 per cent of the stellar masses derived for the galaxies in these regions, indicating that the presence of gas should not affect black hole mass estimates based on the dynamical modelling of the stars. The high spatial resolution provided by the SINFONI data allowed us to resolve a circumnuclear ring (with a radius of ∼270 pc) in the galaxy NGC 4536. The measured values of the Brγ equivalent width and the He I/Brγ emission-line ratio suggest that bursts of star formation occurred throughout this ring as recently as 6.5 Myr ago.

Key words: line: formation – ISM: molecules – galaxies: ISM – galaxies: nuclei – infrared: galaxies.

1 INTRODUCTION

It is widely accepted that supermassive black holes (SMBHs), with masses between 10^6–10^{10} $M_\odot$, sit at the centre of elliptical galaxies and bulges of spiral galaxies. The observational correlation between the mass of the central black hole (M_{BH}) and the bulge mass or the luminosity and the velocity dispersion (σ) of the galaxy's bulge, strongly suggests a connection between the formation of the central black holes (BHs) and the formation and evolution of their hosts (e.g. Kormendy & Richstone 1995; Magorrian et al. 1998; Ferrarese & Merritt 2000; Gebhardt et al. 2000; Tremaine et al. 2002; Marconi & Hunt 2003; Häring & Rix 2004; Gültekin et al. 2009). However, the universality of these relationships has not yet been firmly established. This is mainly due to the fact that they are still based on a limited sample of galaxies, biased towards early types.

In this spirit, an observational spectroscopic survey of nearby galaxies, using the near-infrared (NIR) integral field spectrograph SINFONI (Eisenhauer et al. 2003; Bonnet et al. 2004) at the Very Large Telescope (VLT), was undertaken. The survey is aimed at increasing the number of M_{BH} estimates to explore the M_{BH}–bulge relations, especially at the poorly known low- and high-mass ends, and testing the BH–bulge formation scenarios. This paper is part of a series reporting the results of the SINFONI programme (Nowak et al. 2007, 2008, 2010; Rusli et al. 2011, 2012a,b; Bender et al. in preparation; Erwin et al. in preparation; Saglia et al. in preparation). A thorough analysis and derivation of BH masses via extensive stellar dynamical modelling can be found in these papers.

⋆ Based on observations at the European Southern Observatory (ESO) Very Large Telescope [083.B-0126(A) and 083.B-0126(B)].
† E-mail: ximena@mpe.mpg.de

Table 1. Log of observations. The columns show the FOV covered by the observations, observing date, on-source exposure time, AO mode (where NGS stands for 'natural guide star' and LGS for 'laser guide star'), estimated FWHM of the PSF and PA of the observation.

Galaxy	FOV (arcsec^2)	Obs. date	$T_{\rm exp}$ (min)	AO mode	PSF (arcsec)	Obs. PA
NGC 3351	3 × 3	2009-04-19	40	LGS	0.20	10
	3 × 3	2009-04-20	40	LGS	0.18	10
	8 × 8	2009-04-21	40	no AO	0.45	10
NGC 3627	3 × 3	2007-03-21	80	LGS	0.24	−12
	3 × 3	2007-03-25	50	LGS	0.27	−12
	8 × 8 (N)	2007-03-25	80	no AO	0.67	−12
	8 × 8 (S)	2009-04-22	20	no AO	0.67	−12
	8 × 8 (S)	2009-05-18	20	no AO	0.59	−12
NGC 4501	3 × 3	2008-03-12	80	NGS	0.13	0
NGC 4536	3 × 3	2009-04-19	60	LGS	0.18	125
	3 × 3	2009-04-22	80	LGS	0.18	125
	8 × 8	2009-04-21	80	no AO	0.74	125
NGC 4569	3 × 3	2008-03-08	80	NGS	0.15	25
NGC 4579	3 × 3	2008-03-08	40	NGS	0.15	96
	3 × 3	2008-03-09	80	NGS	0.15	96

Of the total sample of galaxies observed with SINFONI, about one-fourth exhibit signatures of gas emission in their nuclei. The gaseous material is considered to be the primary fuel source of the nuclear activity. It is not only necessary for the formation and growth of the nuclear BHs but it is also a fundamental ingredient for the nuclear and circumnuclear starburst activity of galaxies. How is the large amount of gas required to fuel the nuclear activity transported to the inner regions of the galaxies? What is the interplay between star formation and central SMBHs? These are among the important questions that need to be answered in order to improve our understanding of galactic nuclei, and are currently the focus of intensive research.

The fuel necessary to drive the nuclear activity has to be transported from galactic scales (∼10 kpc) to scales of less than 1 kpc and into the nucleus. Depending on the scales involved, a number of mechanisms that remove angular momentum from the gas, thus bringing it closer to the centre, have been proposed (see review by Jogee 2006 and references therein). Large-scale bars (and the star-forming rings sometimes associated with them), as well as tidal interaction and mergers, seem to play a key role in the transport of the gas into the inner kpc. On smaller scales, nuclear nested bars (e.g. Shlosman, Frank & Begelman 1989) and nuclear spirals (e.g. Englmaier & Shlosman 2000; Maciejewski 2004a,b) are some of the means of removing angular momentum that have been proposed.

The study of the distribution and properties of the molecular gas and star-forming regions in galactic nuclei can provide clues on the mechanisms channelling the gas to the centre and thus fuelling nuclear activity, and can also help establish the link between the starburst and nuclear SMBHs. The SINFONI data set is ideal for this task, since it simultaneously provides high spatial resolution and the advantages of NIR wavelengths, like low dust extinction and a number of emission lines that can be used as diagnostic for the properties of the molecular gas and the nuclear activity.

This is the first of two papers presenting new integral field spectroscopic (IFS) data for six of the galaxies that show molecular emission in our SINFONI sample of 33 galaxies.[1] Both are aimed at characterizing the properties of the nuclear gas and determining its effect on (and possible use in) the estimation of the mass of the central BH. Here, we focus on the emission-line gas distribution and mass content of the galaxies, considering the implications for the estimation of BH masses. In a second paper (Mazzalay et al., in preparation), the kinematics of the gas is analysed and compared with that of the stars. The layout of this paper is as follows. In Section 2, we describe the new SINFONI observations and the data-reduction process. In Section 3, we describe the main properties of the galaxies in the sample and analyse the morphology of the nuclear regions. Section 4 presents the results on the physical conditions of the molecular and ionized gas. An inventory of the total (gas plus star) mass content is given in Section 5. A summary and our main conclusions can be found in Section 6.

[1] Two further galaxies, NGC 1316 and NGC 3368, show molecular emission and were discussed by Nowak et al. (2008, 2010).

2 OBSERVATIONS AND ANALYSIS OF THE DATA

2.1 IFS observations

The data presented here were gathered as part of our observational campaign to measure SMBH masses using the NIR integral-field spectrograph SINFONI at the 8 m VLT UT4. The galaxies were observed in several runs between 2007 and 2009. A short description of the observations can be found in Table 1. We covered the 1.95–2.45 μm wavelength range with the *K*-band grating using two different spatial samplings: a high-spatial-resolution scale of 0.05 × 0.10 arcsec^2 pixel^{-1} (hereafter HR data) and a low-resolution scale of 0.125 × 0.250 arcsec^2 pixel^{-1} (hereafter LR data). The associated fields of view (FOVs) are approximately 3 × 3 and 8 × 8 arcsec^2, respectively. The observations were performed following a standard object-sky-object strategy, with individual exposures of 10 min dithered by a few spatial pixels (or 'spaxels'). This procedure allows a good correction of bad pixels and cosmic ray removal. The total on-source exposure times are listed in column 4 of Table 1. The high-spatial-resolution observations were AO-assisted, employing either the laser guide star (LGS) PARSEC (Rabien et al. 2004) or the natural guide star (NGS) mode using the galaxy nucleus, while the low-resolution observations were taken in natural seeing. In order to assess the AO performance and characterize the point spread function (PSF) due to atmospheric turbulence, we regularly observed a PSF star immediately after the science exposure sequence, in addition to the normal (non-AO) observation of a

telluric standard star. The PSF stars for individual galaxy observations were chosen to have optical ($B - R$) colours and R-band magnitudes similar to that of the inner $r < 3$ arcsec of the galaxy nuclei, in order to achieve a similar AO correction. Column 6 of Table 1 lists the full width at half-maximum (FWHM) of the PSF star associated with each AO-assisted observation and, for the cases of the non-AO observations, the seeing values at 2.2 μm estimated from those given by the Differential Image Motion Monitor (DIMM). Note that, since the DIMM seeing is measured at 0.5 μm, we assumed that the resolution θ depends on the wavelength as $\theta(\lambda) \sim \lambda^{-1/5}$ in order to have an estimation of the seeing at 2.2 μm. Both high- and low-spatial-resolution configurations give a spectral resolution $R \sim 4000$ at 2.12 μm, corresponding to an instrumental dispersion of $\sigma_{\rm ins} \sim 30$ km s^{-1}.

2.2 Data reduction

The data were reduced using a custom pipeline incorporating ESOREX (Modigliani et al. 2007) and SPRED (Schreiber et al. 2004; Abuter et al. 2006). The reduction process comprised all standard reduction steps, including bias subtraction, flat-fielding, bad pixel removal, detector distortion and wavelength calibrations, sky subtraction (Davies 2007), reconstruction of the object data cubes and, finally, telluric and flux calibrations. Through the reduction tasks, the data cubes were re-sampled to a spatial scale of 0.05×0.05 and 0.125×0.125 arcsec^2 pixel^{-1} for the HR and LR data, respectively. Telluric correction and flux calibration of the reconstructed data cubes were performed using the telluric standard stars observed at the beginning or the end of the corresponding observing block at an airmass similar to that of the galaxy. Each star spectrum was extracted from an aperture with a diameter of five to seven times the mean FWHM and its continuum was modelled with a blackbody curve of the same effective temperature and K magnitude as the star. To test our flux calibration, we used 2MASS images in combination with high-resolution *Hubble Space Telescope* (*HST*; NIC2 and NIC3) and William Herschel Telescope (WHT) NIR images available for NGC 3351, NGC 4569 and NGC 4579. The images were obtained from the *HST* archive, NASA/IPAC Infrared Science archive and Knapen et al. (2003). We find an agreement between the different data sets consistent to 20 per cent.

2.3 Construction of the 2D maps

The SINFONI data presented here allow us to study the morphology and physical conditions of the circumnuclear molecular gas of the galaxies in the sample. To improve the signal-to-noise ratio (SNR) of the 2D data and, at the same time, preserve the highest possible spatial resolution, we used the adaptive 2D-binning method of Cappellari & Copin (2003). This method makes use of Voronoi tessellations to bin pixels together by accreting new pixels into the bin until a desired SNR is reached. Here, the SNR was defined as the ratio between the flux of the particular emission line analysed and the rms of the continuum, optimally weighted as described in section 2.1 of Cappellari & Copin (2003). The chosen SNR threshold depended on each individual galaxy and was selected so as not to compromise spatial resolution in the high-SNR regions and, at the same time, be able to extract information from the regions which showed signs of emission but too low SNR to obtain otherwise meaningful line parameters.

In order to extract information about the molecular gas we fitted a Gaussian component to the H_2 2.12 μm emission line in the continuum-subtracted spectra of the galaxies, obtaining the central wavelength, width and intensity of the line at each spatial bin. This line was selected since it is one of the strongest H_2 lines observed in the K-band range and it is located in a region not contaminated by other spectral features. We used the measured intensity to construct emission-line flux distribution maps of the H_2 emission-line gas. The stellar continuum was fitted and subtracted applying the penalized pixel fitting method of Cappellari & Emsellem (2004). For this we used a stellar template constructed as a positive linear combination of the spectra of six late-type stars observed with the same configuration as the galaxy data (in this way we ensure that the stellar template and the objects spectra have the same instrumental broadening). Particular care was taken in masking regions contaminated by emission lines and/or spurious features (i.e. bad pixels or bad sky-lines subtraction).

Visual inspection of the emission-line profiles showed no significant deviation from a single Gaussian component for all the galaxies except NGC 4579. The H_2 emission-line profiles of this galaxy display strong asymmetries and double components in some regions. In consequence, to obtain a good estimation of the total integrated line flux for this galaxy, we described its line profiles as the sum of two Gaussian components. The resulting maps of H_2 2.12 μm flux distribution are shown and analysed in the next section.

Additionally, Brγ emission was observed in the spectra of NGC 3351, NGC 3627 and NGC 4536, and the He I 2.06 μm emission line was present in the spectra of NGC 4536. Following the same procedure as in the case of H_2, we constructed the flux distribution maps for these lines and included their analysis in the next section.

As an example, Fig. 1 shows the integrated continuum-subtracted spectrum of the inner $\sim 8 \times 8$ arcsec^2 of NGC 4536 obtained in the LR configuration.

3 MORPHOLOGY OF THE CIRCUMNUCLEAR GAS

All the galaxies discussed in this paper display H_2 emission lines in their spectra and, in some cases, Brγ and He I 2.06 μm emission were also observed. In this section, we describe and analyse the emission-line flux distribution maps of each individual galaxy, as well as relevant previous observations which will allow us to understand the context in which these data reside. All the SINFONI maps are centred at the K-band continuum maximum; the continuum was estimated by integrating the signal in the 2.1–2.3 μm wavelength range. The main properties of the galaxies are summarized in Table 2. The inclination and position angles (PA) of the galaxies were derived from a combination of analysis of the shape of outer galaxy isophotes and (where available) large-scale gas kinematics in the literature; details for individual galaxies will be presented in Erwin et al. (in preparation).

3.1 NGC 3351

NGC 3351 (M95) is one of the main members of the Leo I group of galaxies and it is classified as an early-type barred spiral galaxy, with no signs of activity in its nucleus. It hosts a star-forming nuclear ring with a major axis of ∼15 arcsec, which dominates the appearance of the inner region of this galaxy, and a larger ring of H II regions that encircles its stellar bar (e.g. Rubin, Peterson & Ford 1975; Devereux, Kenney & Young 1992; Colina et al. 1997; Knapen, Pérez-Ramírez & Laine 2002). Aligned almost perpendicular to the stellar bar, a nuclear 'molecular gas bar' ∼19 arcsec long was first reported by Devereux et al. (1992). Higher spatial resolution

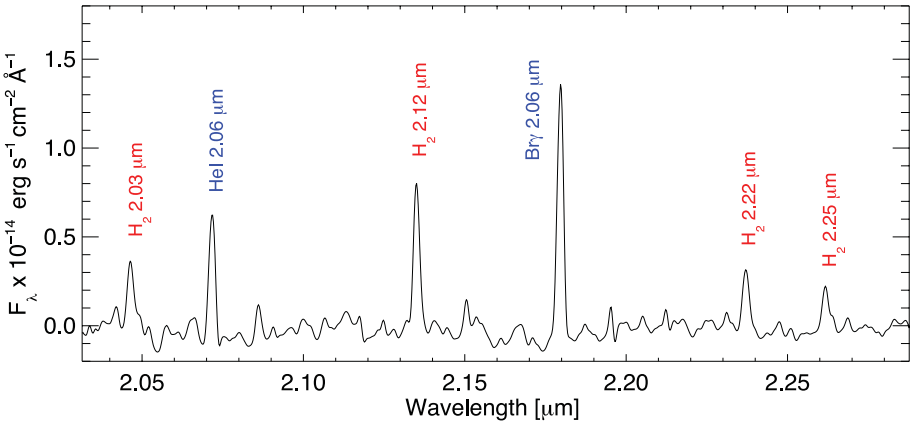

Figure 1. Continuum-subtracted SINFONI spectrum of the inner 8×8 arcsec^2 of NGC 4536. The labels mark the position of the emission lines identified.

Table 2. Properties of the galaxies of the sample.

	NGC 3351	NGC 3627	NGC 4501	NGC 4536	NGC 4569	NGC 4579
Morphology[a]	SB(r)b	SAB(s)b	SA(rs)b	SAB(rs)bc	SAB(rs)ab	SAB(rs)b
Nuclear activity	–	LINER/Sy2[a]	Sy2[a]	LLAGN[b]	LLAGN[c]	LINER/Sy1.9[c]
Distance (Mpc)	10.0[d]	10.1[d]	16.5[e]	14.9[d]	16.5[e]	16.5[e]
Linear scale (pc arcsec^{-1})	49	49	80	72	80	80
Inclination (deg)	46	65[c]	60	69	69	40
PA (deg)	10	178[f]	140	125	25	95
PA of the stellar bar (deg)	112[g]	161[h]	–	–	15[i]	58[j]

[a]Taken from NED. [b]McAlpine et al. (2011). [c]Ho, Filippenko & Sargent (1997). [d]Freedman et al. (2001). [e]Mean Virgo cluster distance (Mei et al. 2007). [f]Casasola et al. (2011). [g]Erwin (2005). [h]Sheth et al. (2002). [i]Jogee, Scoville & Kenney (2005). [j]García-Burillo et al. (2005).

observations resolved this into two peaks of CO emission at a radius of ∼7 arcsec, coincident with the circumnuclear ring observed in Hα images (Jogee et al. 2005).

NGC 3351 was observed with SINFONI in two different configurations, with high- and low-resolution spatial samplings, covering $\sim 3 \times 3$ and $\sim 8 \times 8$ arcsec^2 FOVs. The H_2 and Brγ flux distribution maps derived from these data sets are presented in Fig. 2. The HR data show that the nuclear emission is resolved into two different clumps embedded in diffuse emission (upper-left panel of Fig. 2). The innermost emission is elongated along the major axis of the galaxy, with a relatively constant flux over the inner ∼1 arcsec and a sharp drop to values below 20 per cent of the flux maximum further out. A smaller off-centre source is located at ∼1 arcsec towards the NW of the nucleus. These two clumps are not individually resolved in the LR data (upper-right panel of Fig. 2), where we can see an almost symmetric central source connected towards the SW by a low-luminosity ridge to the inner edge of the nuclear ring observed in Hα and UV images (Colina et al. 1997; Planesas, Colina & Perez-Olea 1997) of this galaxy. Although only part of the ring falls within the SINFONI field, the observed H_2 and Brγ distribution found here agrees very well with previous observations of Hα emission-line maps, especially at the location of the hotspots. The brightest Brγ emission can be associated with the Hα hotspot labelled as R2 by Planesas et al. (1997) and the emission observed at the east edge of the SINFONI field can be associated with the R5, R6 and R7 Hα hotspots (see fig. 8 of Planesas et al. 1997). However, the Brγ map does not show the nuclear emission observed in both the H_2 maps presented here and previous Hα images. This is probably due to the intrinsic weakness of the Brγ line, which falls below the sensitivity limit of our data. Hints of nuclear Brγ emission are observed in the inner ∼1 arcsec of the HR spectra, although it is not strong enough to allow the construction of an emission-line map.

3.2 NGC 3627

NGC 3627 (M66) is a high-inclination strongly barred galaxy. It belongs to the Leo Triplet group of galaxies, showing some signatures of past interaction with its neighbour galaxy NGC 3628. Optical emission-line ratios are inconclusive with respect to the type of nucleus this galaxy harbours. Whether it is a LINER/H II composite or Seyfert 2 like nucleus (Ho et al. 1997), the presence of a variable, flat-spectrum nuclear radio source is consistent with a low-luminosity AGN (LLAGN, Filho, Barthel & Ho 2000). Broad-band optical images of NGC 3627 reveal a pronounced spiral pattern and a central region dominated by several straight dust lanes that run parallel to the host galaxy semimajor axis (Martini et al. 2003). The CO emission shows a nuclear peak and extends along the leading edges of the stellar bar, forming two broad peaks at the bar ends, from where the spiral arms trail off (e.g. Sheth et al. 2002).

Molecular and recombination lines of hydrogen were observed in the SINFONI spectra of NGC 3627. The left-hand panels of Fig. 3 show the flux distribution maps of the H_2 2.12 μm and Brγ lines in the inner $\sim 3 \times 3$ arcsec^2 (HR maps) of this galaxy. Additionally, two sets of low-resolution observations were taken with a spatial offset along the -12° PA, yielding a total FOV of $\sim 8 \times 15$ arcsec^2. The final H_2 distribution map obtained from these data (LR map) is presented in the right-hand panel of Fig. 3. No evidence of Brγ emission was found at distances larger than a few arcseconds from

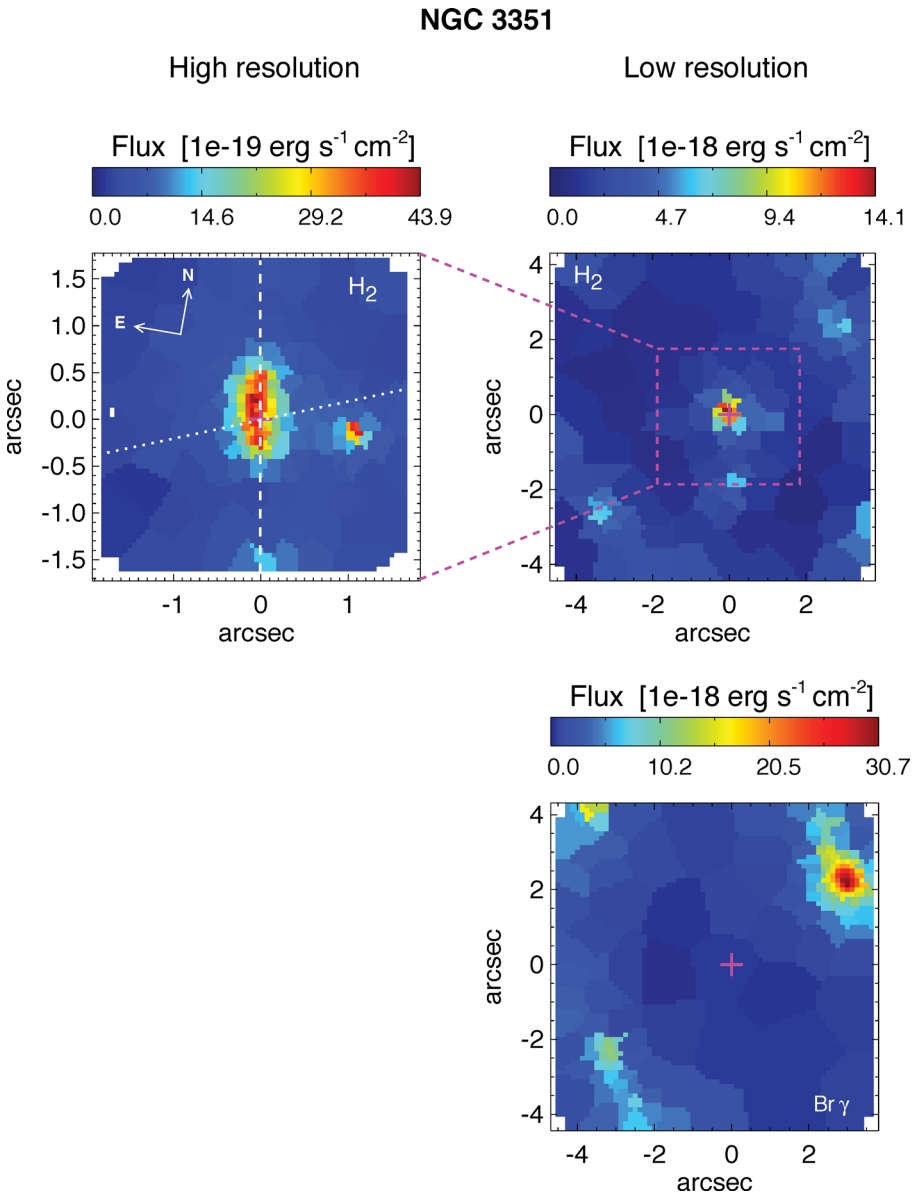

Figure 2. Flux distribution of H_2 2.12 μm (upper panels) and Brγ (lower panel) emission lines observed in NGC 3351. The panel on the left corresponds to the high-resolution data (FOV $\sim 3 \times 3$ arcsec^2) and the panels on the right correspond to the low-resolution data (FOV $\sim 8 \times 8$ arcsec^2). The spatial orientation, indicated in the upper-left panel, is the same for all the panels. The position of the major axis of the galaxy (dashed line) and the orientation of the stellar bar (dotted line) are also indicated.

the nucleus; therefore, we only show its distribution derived from the HR data.

As it can be seen from Fig. 3, while the emission of Brγ appears strictly confined to the nucleus, within a region of $\lesssim$50 pc in radius, the morphology of the H_2 emission in the inner 3×3 arcsec^2 is extended along N–S direction. Further out, the gas is mainly located along a bar-like structure, with two hotspots located approximately at distances of 6.5 and 4.5 arcsec from the nucleus along a PA of $\sim$17° (from north through east). Additionally, weak emission extending southwards is observed beyond the southern hotspot. The morphology displayed by the H_2 emission line is remarkably consistent with the ^{12}CO(2–1) morphology reported by Casasola et al. (2011) for the inner 20×20 arcsec^2 of NGC 3627 (see their fig. 4). The PA of the molecular bar-like structure observed in the innermost regions of NGC 3627 differs from the PA of the stellar bar (PA = 161°, indicated with a dotted line in Fig. 3) and the large-scale molecular bar (PA = 164°; Sheth et al. 2002). This is because we are looking well within the transition region, where the molecular gas goes from leading the northern part of the stellar bar to lead the southern one (see, for example, fig. 1 of Regan et al. 2001).

3.3 NGC 4501

The Seyfert 2 galaxy NGC 4501 (M88) is one of the largest spiral galaxies in the Virgo cluster region. *B*-band images presented by Elmegreen & Elmegreen (1987) showed multiple external arms and two symmetric inner arms. In the *K*′-band, the spiral structure is continuous within $r \lesssim 3$ kpc (Elmegreen et al. 1999) and Carollo, Stiavelli & Mack (1998) were able to observe spiral-like dust lanes

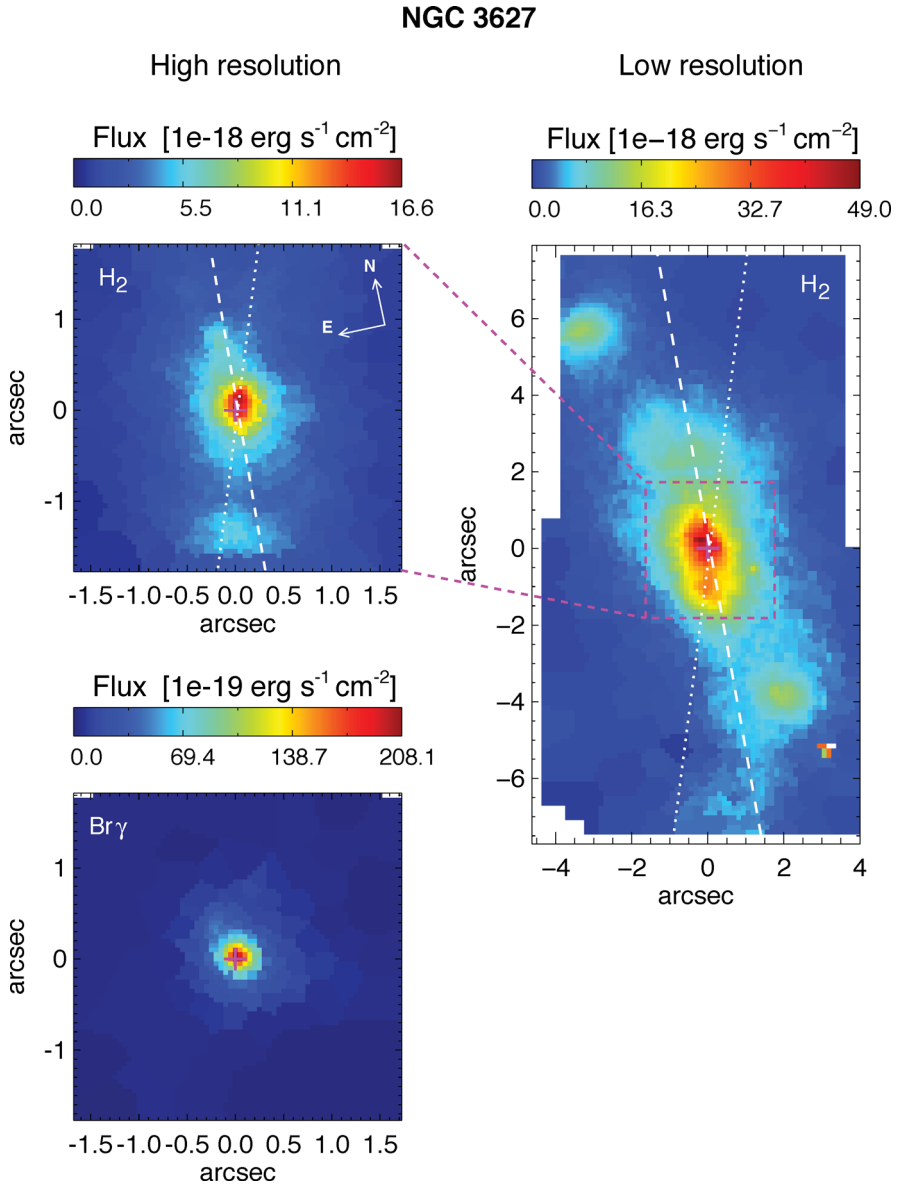

Figure 3. Flux distribution maps of the H_2 and Brγ emission lines observed in NGC 3627. The panels on the left correspond to the high-resolution data and the panel on the right corresponds to the low-resolution data. The spatial orientation, indicated in the upper-left panel, is the same for all the panels. The dashed line in the H_2 maps indicates the position of the major axis of the galaxy and the dotted line corresponds to the stellar bar PA.

(thought to indicate the location of shocks) down to the nucleus, using WFPC2 F606W images. High-resolution interferometric observations of the ^{12}CO(1–0) emission in the central 5 kpc of this galaxy were analysed in detail by Onodera et al. (2004). The CO maps showed spiral arms, associated with the dust lanes found by *HST*, and a strong central condensation of radius ∼5 arcsec resolved into double peaks separated by 4.7 arcsec, which are located on the 'root of the dust spirals'. Even though NGC 4501 does not show evidence for a bar, the gas concentration in its centre is relatively high, and more typical of barred than unbarred galaxies (Sakamoto et al. 1999a).

Fig. 4 shows the flux distribution map of the H_2 2.12 μm emission line in the inner 3×3 arcsec^2 of NGC 4501 observed with SINFONI. Two distinct structures can be resolved in the integrated flux map: an asymmetric nuclear component (note that the maximum of the H_2 emission is offset from the continuum maximum indicated by the plus symbol) surrounded by two arcs that resemble an incomplete ring-like structure. The arcs traced by H_2 towards the NW and SE of the nucleus seem to be located on the inside edges of the two peaks seen in CO by Onodera et al. (2004), indicating a gradient in the temperature of the molecular gas in the sense that the warm molecular gas (traced by the H_2 2.12 μm emission) is located closer to the nucleus than the cold molecular gas (traced by the CO emission). A comparison between the H_2 emitting gas distribution and the nuclear spiral-like dust lanes exhibit by NGC 4501 can be seen in Fig 5. This figure shows an unsharp mask of the *HST*/WFPC2 F547M image (retrieved from the *HST* archive) of the inner regions of the galaxy, with the H_2 contours overlaid. As in the case of the CO emission, a close spatial coincidence between the H_2 molecular gas and the dust lanes is observed, especially in the north region where both the molecular and dust structures are better defined, suggesting a close relation between

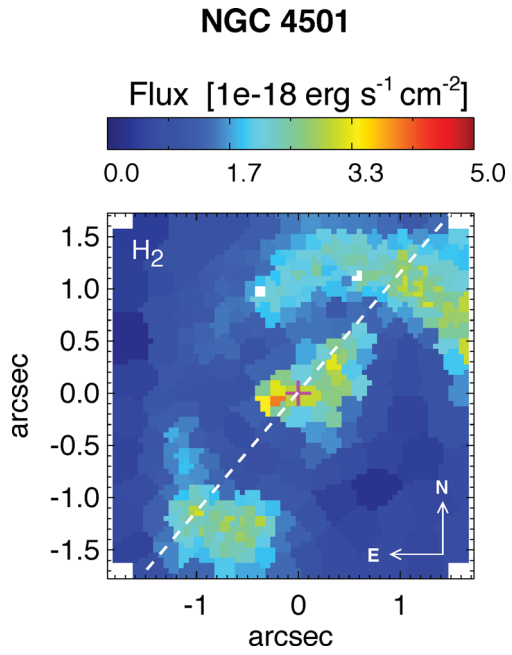

Figure 4. Flux distribution map of the H_2 emission line observed in NGC 4501. The dashed line represents the orientation of the major axis of the galaxy.

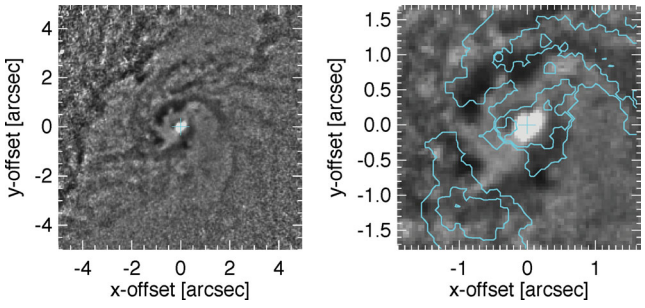

Figure 5. Left: unsharp mask of the *HST*/WFPC2 F547M image of the inner 10×10 arcsec^2 of NGC 4501. The dust lanes trace spiral patterns around and to the nucleus. Right: zoom into the inner 3×3 arcsec^2 with the H_2 contours overlaid.

the two media down to distances of less than 1 arcsec from the nucleus.

3.4 NGC 4536

NGC 4536 is a large spiral galaxy located in the Virgo cluster. While it has been classified as an SAB(rs)bc galaxy (e.g. de Vaucouleurs et al. 1991; Buta et al. 2010), the evidence for the presence of a bar is not yet clear (see for example Pompea & Rieke 1990; Shaw et al. 1995, Erwin et al. in preparation). Although optical line ratios place this galaxy in the H II region range (Ho et al. 1997), the presence of high-ionization lines (Satyapal et al. 2008) and its X-ray spectrum (McAlpine et al. 2011) suggest that this galaxy hosts an LLAGN in its nucleus. Additionally, there is abundant evidence pointing to vigorous star formation taking place in the inner $\sim 20 \times 30$ arcsec^2 region of this galaxy (e.g. Puxley, Hawarden & Mountain 1988; Pogge 1989; Telesco, Dressel & Wolstencroft 1993; Davies, Sugai & Ward 1997; Jogee et al. 2005). This is also a typical 'single-peak' type galaxy, with the CO molecular gas being concentrated in a nuclear disc of $\sim$10 arcsec radius and an unresolved compact core at the nucleus (e.g. Sofue et al. 2003; Jogee et al. 2005). Previous low-resolution (1.6 arcsec) images of H_2 2.12 μm emission in the inner 10 arcsec of this galaxy were analysed by Davies et al. (1997). They found a strong NIR continuum peak in the nucleus, but the H_2 emission has peaks distributed in what seems to be an edge-on ring structure around the nucleus. Their analysis suggests that while active star formation is taking place in the circumnuclear ring, the star formation in its nucleus has come to an end (see also Jogee et al. 2005). Very recently, Rosenberg, van der Werf & Israel (2012) presented non-AO *H*-, *J*- and *K*-band SINFONI data of the inner 8×8 arcsec^2 of NGC 4536. These authors confirmed the presence of a circumnuclear ring in NGC 4536, traced mainly by Brγ and [Fe II] 1.26 μm emission, while the H_2 2.12 μm distribution is more centrally peaked.

High- and low-resolution data of the nuclear region of NGC 4536 were obtained with SINFONI, covering the inner 3×3 and 8×8 arcsec^2, respectively. Intense Brγ and H_2 emission lines were detected in the spectra of this galaxy, together with weaker He I 2.06 μm emission. The flux distribution maps of H_2 2.12 μm, Brγ and He I derived from the SINFONI data are shown in Fig. 6. The left-hand panels correspond to the maps derived from the high-resolution data (HR maps) and the right panels show the ones derived from the low-resolution data (LR maps).

It can be seen in Fig. 6 that the circumnuclear molecular and atomic gas of NGC 4536 exhibit very different morphologies. The Brγ emission is mainly localized in a circumnuclear ring $\sim$7.5 arcsec (540 pc) in diameter, oriented along the photometric semimajor axis of the galaxy. The ratio between the semimajor and -minor axes of the ring ($\sim$2.8) is consistent with a circular ring with the same inclination as the galaxy ($i = 69^\circ$, Table 2) projected on to the sky. The Brγ emission is not uniformly distributed along the ring but shows a knotty appearance, with the strongest emission located towards the NW. In contrast, the H_2 emission is more centrally concentrated, with the bulk of the emission restricted to the inner $\sim$2 arcsec of the galaxy. The detailed structure of this region can be seen in the HR H_2 distribution map, which shows that the H_2 emission does not peak at the position of the active nucleus but seems to encircle it. The nuclear region is connected to the circumnuclear ring by two ridges of weak H_2 emission extending towards the south and the north, giving a global S-shaped appearance to the H_2 distribution. In general, the morphologies of the H_2 and Brγ emission lines showed by the LR maps are consistent with those presented by Rosenberg et al. (2012). The presence of strong H_2 emission in the nucleus of NGC 4536 and the absence of strong hydrogen recombination lines (i.e. Brγ) support the scenario proposed by Davies et al. (1997), in which no current star formation is taking place in the nuclear region of this galaxy (see Section 4.2 for a detailed discussion).

NGC 4536 is the only galaxy in the sample for which He I 2.06 μm line emission was observed. The morphology of the He I line-emitting gas (lower-right panel of Fig. 6) has an almost perfect one-to-one correspondence with the Brγ emission, indicating that both Brγ and He I are tracing the same structures.

While previous low-resolution observations suggested the presence of a circumnuclear ring in this galaxy (e.g. Vila et al. 1990; Davies et al. 1997; Laine et al. 2006), the high spatial resolution provided by SINFONI gives a clear view of the circumnuclear ring present in the inner $\sim$8 arcsec of NGC 4536. A more detailed study of the ionized gas ring of this galaxy is presented in Section 4.2.1.

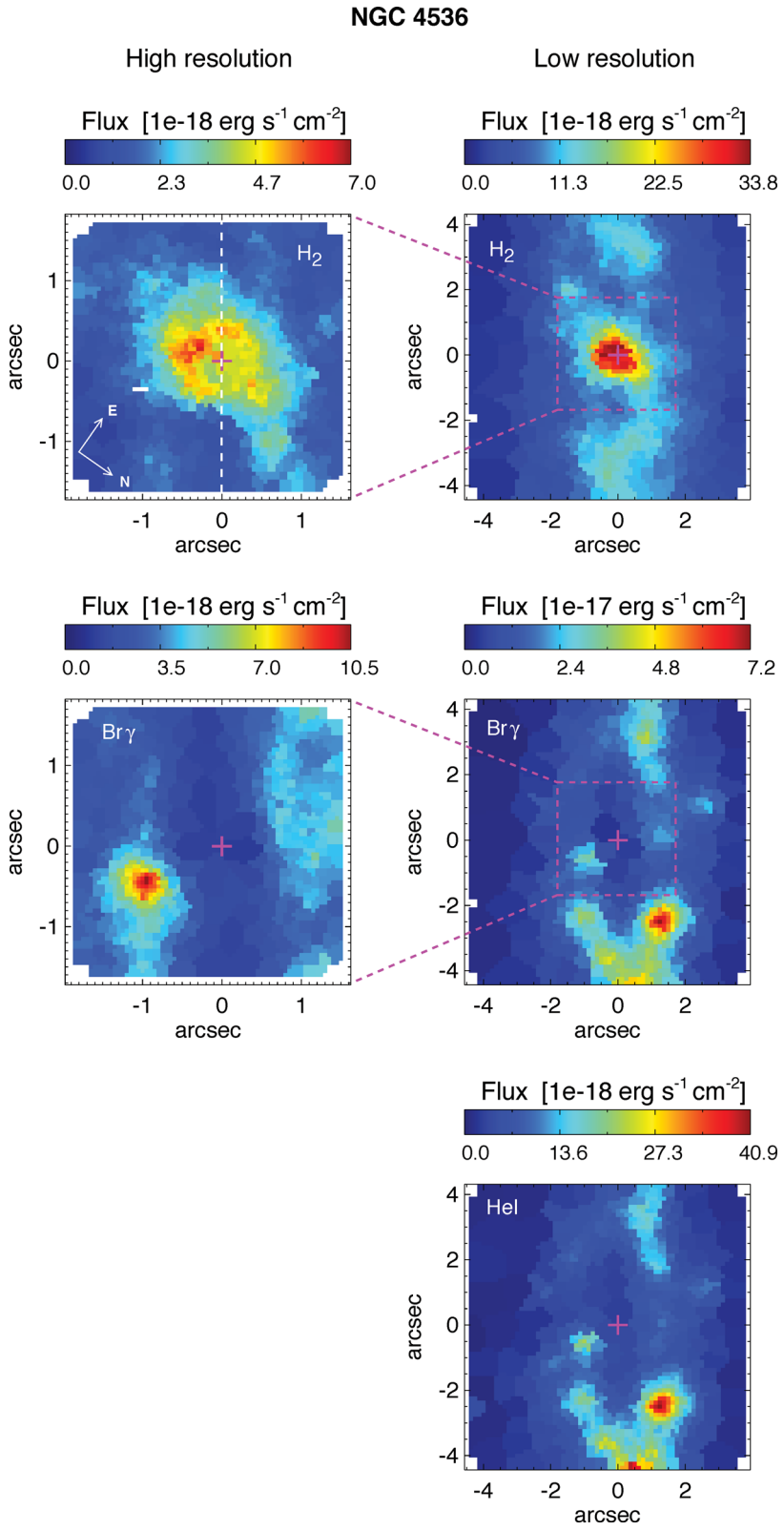

Figure 6. Flux distribution maps of the H_2 2.12 μm (upper panels), Brγ (middle panels) and He I 2.06 μm (lower panel) emission lines observed in NGC 4536. Left-hand panels correspond to the high-spatial-resolution data and right-hand panels to the low-spatial-resolution data. The spatial orientation, indicated in the upper-left panel, is the same for all the panels. The dashed line in the upper-left panel represents the orientation of the major axis of the galaxy.

3.5 NGC 4569

NGC 4569 (M90) is a member of the Virgo cluster classified as an SAB(rs)ab galaxy. Its nucleus was classified as a 'transition object' or weak-[O I] LINER by Ho et al. (1997), although the mechanism producing the nuclear activity is still unclear, with several lines of evidence indicating a strong contribution from a nuclear starburst (e.g. Keel 1996; Ho et al. 1997, 2001; Maoz et al. 1998; Alonso-Herrero et al. 2000; Barth & Shields 2000; Gabel & Bruhweiler 2002). This galaxy has a bright, point-like nucleus at optical and *UV* bands that dominates the emission. The *HST* $V - I$ map shows that while the circumnuclear region is dusty, the nucleus itself is apparently unobscured by dust (Pogge et al. 2000). NGC 4569 is considered an 'anemic spiral' because of its H I deficiency (it has $\sim$1/10 of the atomic gas that similar field galaxies have) and small extent compared to its optical size (e.g. van den Bergh 1976; Cayatte et al. 1994; Koopmann & Kenney 2004). Its molecular CO gas has been extensively studied (e.g. Kenney & Young 1986; Sakamoto et al. 1999a,b; Helfer et al. 2003; Sofue et al. 2003; Jogee et al. 2005; Nakanishi, Sofue & Koda 2005; Boone et al. 2007, 2011; Wilson et al. 2009). The CO emission is highly concentrated in a compact bar-like region (of $\sim 17 \times 6$ arcsec^2 extending along PA $\approx$ 24°) with three off-centre peaks, one located at $\sim$1 arcsec towards the north-east of the nucleus and two symmetrical peaks separated by $\sim$10 arcsec (Boone et al. 2007).

The SINFONI observations of NGC 4569 were done in the high-resolution configuration, covering a total FOV of 3×3 arcsec^2. The *K*-band emission-line spectrum of this galaxy is dominated by H_2 transitions, with no signs of emission from ionized gas. This is consistent with previous long-slit observations where no Paβ and/or Brγ emission was detected in the nucleus (e.g. Alonso-Herrero et al. 2000; Rhee & Larkin 2005). Fig. 7 shows the H_2 flux distribution map derived from H_2 2.12 μm. It can be seen that the H_2 emission-line gas distribution is very irregular, with most of the emission located off-nucleus on the eastern part of the FOV. There is a rapid drop in the SNR as one goes from the eastern and southern regions towards the north, where the intensity of the H_2 line falls below the continuum noise level. Although the SINFONI data presented here are mapping only a small part of the molecular bar observed in NGC 4569, it is possible to say that the general H_2 distribution displayed by this galaxy is consistent with the CO(1–0) and CO(2–1) maps reported by Boone et al. (2007), in the sense that the stronger emission is located towards the east and south. However, the H_2 emission peaks closer to the nucleus than the CO emission, suggesting a strong gradient in the molecular gas temperature going from the centre to the outer regions of the galaxy.

3.6 NGC 4579

NGC 4579 is an SAB(rs)b galaxy with a LINER/Seyfert 1.9 nucleus (Ho et al. 1997). As in the case of NGC 4569, this galaxy is considered an 'anemic spiral' of the Virgo cluster. *HST* UV, [O III] and Hα images show a bright nuclear point source surrounded by filamentary structures, with the brightest emission located at distances $\lesssim$2 arcsec towards the NE (Maoz et al. 1995; Pogge et al. 2000). High-resolution CO intensity maps presented by García-Burillo et al. (2005, 2009) showed that most of the cold molecular gas in NGC 4579 is located in a two spiral arm structure that can be traced from $r \sim 10$ arcsec down to a distance of 2 arcsec from the nucleus. The spiral arms lie at the leading edges of the $\sim$12 kpc-diameter bar identified in *K*-band images (e.g. Knapen et al. 2003) and are well correlated with dust lanes revealed by $V - I$ *HST* images (Pogge et al. 2000), especially the arm located towards the north. Some emission from CO is observed at smaller distances from the centre but not on the position of the AGN itself.

The SINFONI *K*-band spectra of the inner 3×3 arcsec^2 of NGC 4579 display strong H_2 emission lines and no evidence of ionized gas. Two main structures are seen in the H_2 emission-line map shown in Fig. 8. This emission is dominated by a symmetric nuclear component, slightly displaced towards the south with

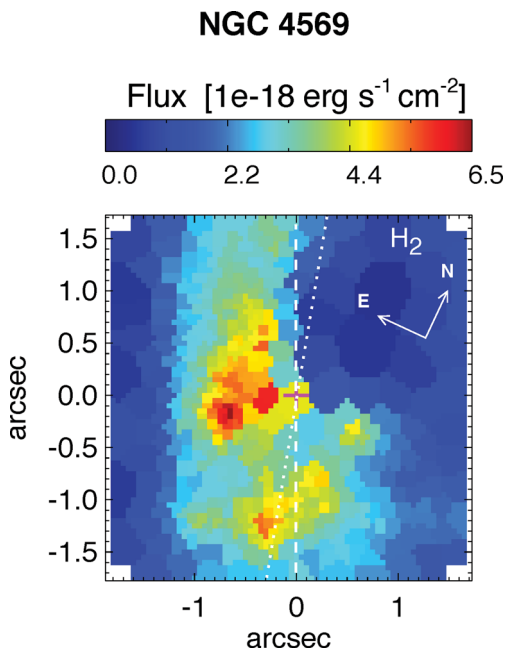

Figure 7. Flux distribution map of the H_2 2.12 μm emission line observed in NGC 4569. The dashed line indicates the position of the major axis of the galaxy and the dotted line corresponds to the stellar bar PA.

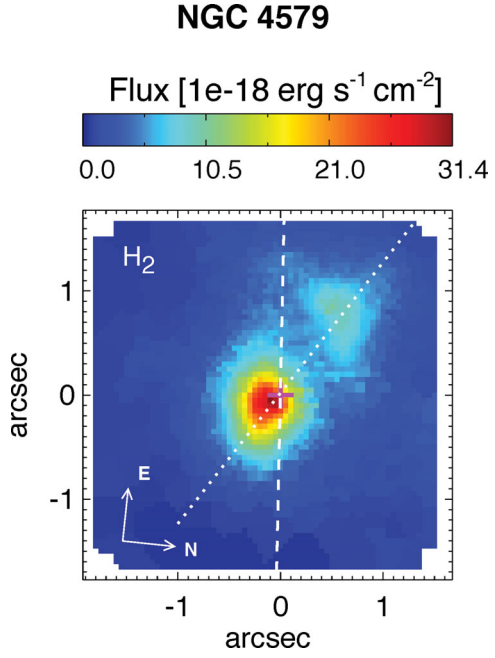

Figure 8. Flux distribution map of the H_2 2.12 μm emission line observed in NGC 4579. The dashed line indicates the position of the major axis of the galaxy and the dotted line corresponds to the stellar bar PA.

respect to the maximum of the continuum. Towards the NE, at a distance of ∼1 arcsec from the nucleus, a weaker component is present. The overall shape of the H_2 emission resembles the one revealed by Hα and [O III] narrow-band images, although the latter show much more complex structures resolved into individual knots (see fig. 1d and 3a of Pogge et al. 2000). Additionally, there is no correspondence between the H_2 emission presented here with dust or CO emission, which is mostly found at larger distances from the nucleus.

4 PHYSICAL CONDITIONS OF THE NUCLEAR REGIONS

Rotational and vibrational H_2 transitions are important cooling channels for warm molecular gas, observed as a series of infrared (IR) emission lines. H_2 emission lines are commonly observed in the NIR spectra of galaxies harbouring energetic processes related to massive star formation, shocks or AGNs, and have proved to be important diagnostic tools in all molecular media.

Most of the galaxies in our sample show signs of AGN activity in their centres and, at the same time, regions where star formation is taking place. Therefore, the data presented here give us an excellent opportunity to study the physical conditions of the H_2 emission-line gas in these two distinct environments. In order to achieve this we extracted spatially integrated 1D spectra from the nuclear and circumnuclear regions of the galaxies. The size and location of these regions vary from galaxy to galaxy depending on their particular morphology and are indicated in the first column of Table 3. Many emission lines were detected in the SINFONI spectra of the sample galaxies, including Brγ and H_2 1.96, 2.03, 2.12, 2.22 and 2.25 μm. As described below, these lines provided us with a variety of tracers of different physical quantities. The emission-line fluxes of the individual lines were obtained by fitting a single Gaussian component plus a linear continuum to the spectra. The LINER routine (Pogge & De Robertis 1993) was used for this purpose. The measured emission-line fluxes can be found in Table 3. The precise position and size of the apertures used to extract the 1D spectra are given in Table A1 of Appendix A.

4.1 Excitation mechanisms and temperature of the H_2 emission-line gas

Several mechanisms have been proposed for the excitation of the ground state ro-vibrational levels of H_2. These can be separated into two main groups: thermal and non-thermal processes. In thermal processes, the H_2 molecule is excited via inelastic collisions with atoms or molecules in warm ($T \sim 500$–2000 K) gas, heated either by shocks or UV/X-ray radiation in high-density regions (e.g. Lepp & McCray 1983; Sternberg & Dalgarno 1989; Brand et al. 1989; Draine & Woods 1990; Maloney, Hollenbach & Tielens 1996). In this case, to a first approximation, the H_2 line-emitting gas is in local thermal equilibrium (LTE) and the spectrum is therefore characterized by a single excitation temperature. Since H_2 is rapidly dissociated by thermal collisions above ∼4000 K, the excitation temperature of the thermal component must be lower than this. In non-thermal processes, the NIR ro-vibrational lines are observed due to a radiative cascade through the excited vibrational and rotational levels of the ground electronic state. The excitation of the electronic state can be produced either by near-UV (11–13.6 eV) pumping to the electronically excited Lyman and Werner bands (e.g. Black & van Dishoeck 1987) or by a collision with a fast

Table 3. Emission-line fluxes (in units of 10^{-16} erg cm^{-2} s^{-1}), temperatures, emission-line ratios and molecular masses measured for different regions of the galaxies of the sample. The errors correspond to 3σ.

Galaxy	H_2 1–0 S(2) 2.03 μm	H_2 1–0 S(1) 2.12 μm	H_2 1–0 S(0) 2.22 μm	H_2 2–1 S(1) 2.25 μm	Brγ 2.16 μm	T_{vib} (K)	T_{rot} (K)	$\frac{H_2\ 2.12\ \mu m}{Br\gamma}$	M_{warm} ($M_\odot$)	M_{cold} ($10^6 M_\odot$)
NGC 3351										
1 – Nucleus	3.9 ± 1.3	7.5 ± 1.6	3.4 ± 1.2	1.2 ± 0.9	1.3 ± 0.9	2600	1125	5.9	3.9	2.8
2 – W cloud	0.7 ± 0.1	1.2 ± 0.2	0.5 ± 0.2	0.2 ± 0.1	–	2800	1500	–	0.6	0.4
3 – 3 × 3 arcsec^2	21.4 ± 5.8	16.7 ± 6.7	11.9 ± 6.7	<6.0	–	<4300	2000	–	8.7	6.2
4 – 8 × 8 arcsec^2	117 ± 55	151 ± 26	54.3 ± 28.7	37.5 ± 28.1	150 ± 25	3300	3000	1.0	79.0	57.0
5 – Ring	–	89.0 ± 22.4	–	–	160 ± 28	–	–	0.56	46.5	33.3
NGC 3627										
1 – Nucleus	18.2 ± 6.9	43.1 ± 6.0	15.0 ± 5.7	6.2 ± 5.7	20.6 ± 6.6	2500	1200	2.1	22.3	16.0
2 – 3 × 3 arcsec^2	41.8 ± 22.9	108 ± 18	32.1 ± 17.4	<17.0	–	<2600	1300	–	55.6	40.0
3 – N cloud	4.7 ± 0.9	11.7 ± 0.5	3.0 ± 0.6	1.3 ± 0.6	–	2207	1680	–	6.0	4.4
4 – S cloud	6.0 ± 0.8	15.2 ± 0.9	4.2 ± 0.9	1.4 ± 1.0	–	2091	1388	–	7.8	5.6
5 – 8 × 15 arcsec^2	–	268 ± 62	–	–	–	–	–	–	138	100
NGC 4501										
1 – Nucleus	–	7.6 ± 3.9	5.8 ± 4.5	–	–	–	–	–	10.5	7.5
2 – Ring	48.1 ± 27.0	50.1 ± 12.9	27.1 ± 18.0	<18.0	–	<4200	2000	–	69.4	49.9
3 – 3 × 3 arcsec^2	–	65.4 ± 20.3	–	–	–	–	–	–	90.6	65.0
NGC 4536										
1 – Nucleus	11.5 ± 6.2	32.6 ± 5.6	17.1 ± 5.9	9.0 ± 5.9	17.0 ± 5.2	3520	730	1.9	37.0	26.6
2 – Ring	92.2 ± 26.0	240 ± 29	105 ± 22	88 ± 25	532 ± 29	4300	885	0.45	272.6	196.0
3 – 8 × 8 arcsec^2	140 ± 59	331 ± 34	151 ± 36	114 ± 36	567 ± 33	4000	920	0.6	375.9	270.0
NGC 4569										
1 – 3 × 3 arcsec^2	52.2 ± 21.2	95.4 ± 18.8	42.5 ± 19.5	24.8 ± 19.5	–	3400	1200	–	74.1	53.3
NGC 4579										
1 – Nucleus	29.5 ± 4.5	46.8 ± 7.5	–	–	–	–	–	–	64.8	46.6
2 – NE cloud	10.2 ± 2.3	19.0 ± 2.4	5.3 ± 2.5	3.0 ± 2.4	–	2600	2300	–	26.4	19.0
3 – 3 × 3 arcsec^2	61.8 ± 25.8	82.9 ± 21.3	34.9 ± 19.7	<22.5	–	3500	>2000	–	114.9	82.6

electron produced by X-ray ionization to singlet electronic states (e.g. Gredel & Dalgarno 1995).

Each of the excitation mechanisms mentioned above produces different H_2 spectra, which are often observed together within a single object (e.g. Mouri 1994; Davies et al. 1997, 2005; Veilleux, Goodrich & Hill 1997; Quillen et al. 1999; Rodríguez-Ardila et al. 2004; Rodríguez-Ardila, Riffel & Pastoriza 2005; Riffel et al. 2006, 2008; Zuther et al. 2007; Storchi-Bergmann et al. 2009; Riffel, Storchi-Bergmann & Nagar 2010). The relative intensity of the H_2 emission lines can be used to infer the dominant process responsible for the H_2 emission. In particular, the H_2 2–1 S(1) 2.25 μm/1–0 S(1) 2.12 μm line ratio is an excellent discriminator between non-thermal and thermal processes, while 1–0 S(2) 2.03 μm/1–0 S(0) 2.22 μm can be used to differentiate between thermal UV excitation and X-ray/shock excitation (Mouri 1994). Additionally, these line ratios are sensitive to the vibrational temperature ($T_{\rm vib}$) and rotational temperature ($T_{\rm rot}$) of the emission-line gas, respectively (e.g. Scoville et al. 1982; Reunanen, Kotilainen & Prieto 2002). The excitation temperature ($T_{\rm vib}$ or $T_{\rm rot}$, depending on the transitions involved) will depend on the relative importance of the radiative and collisional processes. In the case of gas in LTE the ro-vibrational level populations are characterized by a thermalized Boltzman population and the excitation temperature corresponds to the kinetic temperature of the gas. Assuming the computed A-Einstein coefficients of Turner, Kirby-Docken & Dalgarno (1977), the relation between the excitation temperature of the gas and the H_2 2–1 S(1)/1–0 S(1) and 1–0 S(2)/1–0 S(0) emission-line ratios can be expressed as

$$T_{\rm vib} \simeq \frac{5600}{\ln\left(1.355 \times \frac{I_{1-0\,{\rm S}(1)}}{I_{2-1\,{\rm S}(1)}}\right)}, \quad (1)$$

$$T_{\rm rot} \simeq \frac{-1113}{\ln\left(0.323 \times \frac{I_{1-0\,{\rm S}(2)}}{I_{1-0\,{\rm S}(0)}}\right)}. \quad (2)$$

Fig. 9 shows the H_2 2–1 S(1)/1–0 S(1) versus 1–0 S(2)/1–0 S(0) line-ratio diagnostic diagram for the selected regions of the galaxies in our sample, together with diverse key excitation models taken from the literature. Each filled symbol represents one particular galaxy and the associated numbers indicate the different regions specified in the first column of Table 3. The right and upper axes show the values of $T_{\rm vib}$ and $T_{\rm rot}$, respectively, derived from equations (1) and (2) as a function of the two line ratios. Table 3 lists the temperature values obtained for the different regions of the galaxies. From this figure it is clear that there is no single excitation mechanism acting in the nuclear and circumnuclear regions of the galaxies, regardless of their type of activity. In general, each region is characterized by a $T_{\rm rot}$ lower than its $T_{\rm vib}$, consistent with some contribution from non-thermal processes. The values of temperature derived vary from ∼700 up to 4000 K, with a tendency for the objects to be located near the pure thermal excitation curve for the range of temperatures ∼1000–3000 K. These high temperatures correspond to the region on the diagram where X-ray/shock thermal excitation dominates. Dors et al. (2012) constructed a grid of photoionization models using the code CLOUDY/08 (Ferland et al. 1998), which includes both collisional and radiative interactions of H_2 and its environment (Shaw et al. 2005). The input parameters are a spectral energy distribution of the ionizing source similar to that observed in typical AGNs, three values of metallicity (0.5, 1 and 2 solar metallicy), an electronic density $n_{\rm e} = 10^4$ cm^{-3} and an ionization parameter U in the $-4.0 \leq \log U \leq -1$ range. The resulting H_2 line ratios span a large range of values, H_2 2.25/2.12 μm ∼ 0.05–0.5 and 2.03/2.22 μm ∼ 1.1–2.0, reproducing most the observed H_2 line ratios of the galaxies in our sample.

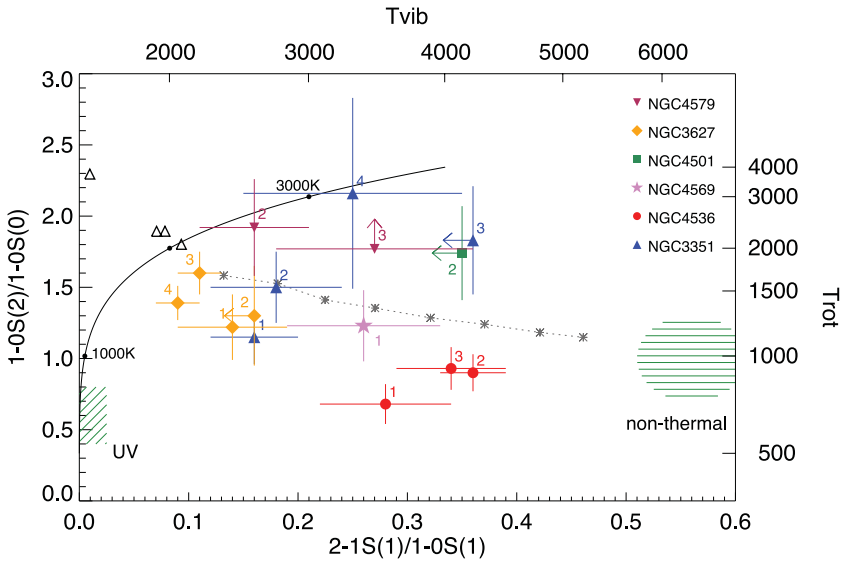

Figure 9. H_2 2–1 S(1) 2.25 μm/1–0 S(1) 2.12 μm and 1–0 S(2) 2.03 μm/1–0 S(0) 2.22 μm emission-line ratios measured from different regions of the galaxies in the sample. The code number of each measurement corresponds to the region of the galaxy specified in Table 3. The solid curve represents thermal emission in the temperature range 500–4000 K (the dots on the curve indicate $T = 1000$, 2000 and 3000 K). The open triangles correspond to X-ray-heating models of Lepp & McCray (1983) and Draine & Woods (1990). Areas of the diagram corresponding to thermal UV excitation models (Sternberg & Dalgarno 1989) and non-thermal UV fluorescence models (Black & van Dishoeck 1987) are indicated with shaded regions. The dashed line represents the predicted line ratios from a mix of thermal and UV-fluorescence models of Black & van Dishoeck (1987), where the percentage of the thermal component decreases in steps of 10 per cent starting at the left with a model where 90 per cent is thermal and 10 per cent is UV fluorescence. Additionally, the corresponding $T_{\rm vib}$ and $T_{\rm rot}$ temperature scales are indicated in the upper and right axes, respectively.

While most of the galaxies in our sample are characterized by a value of H_2 2.03/2.22 μm higher than 1, this ratio is lower in the case of NGC 4536. The H_2 line ratios of this galaxy occupy a region on the diagram dominated by a mix of UV thermal and non-thermal models, suggesting that UV radiation plays a key role in the excitation of the H_2 in this galaxy, with no significant contribution from shocks and/or X-ray radiation. The combination of low T_{rot} and high T_{vib} makes this galaxy unique among the objects presented here, placing it in a region of the diagram typically occupied by photodissociation regions.

In summary, the analysis presented in this section suggest that thermal processes are primarily responsible for the excitation of the H_2 gas in the nuclear and circumnuclear regions of the galaxies in our sample, with some minor contribution from non-thermal processes (i.e. UV fluorescence).

4.2 Ionized gas and the H_2/Brγ emission-line ratio

The Brγ recombination line was observed in half of the galaxies of the sample and, even though the number of objects is low, we can appreciate very different morphologies displayed by this line. In two cases (NGC 3351 and NGC 4536) the flux distribution maps of Brγ show a clear ring-like morphology, while in the third case (NGC 3627) the bulk of emission is restricted to a relatively compact nuclear region.

In general, the Brγ distribution of the galaxies in the sample does not follow their H_2 emission. A clear deficit of Brγ emission relative to the H_2 emission is observed in the nuclei of NGC 3351 and NGC 4536. In order to quantify this, we included in Table 3 the values of the H_2 2.12 μm/Brγ emission-line ratio measured for the different regions of the galaxies. These values vary between 0.45 and 5.9, in agreement with the usual values found for starburst galaxies and AGNs (e.g. Larkin et al. 1998; Moorwood & Oliva 1988, 1990; Rodríguez-Ardila et al. 2004, 2005; Riffel et al. 2010). The expected line ratio for starburst-dominated galaxies is typically low ($\lesssim$0.6), while LINER nuclei show the highest ratios, usually $\gtrsim$2. Composite and Seyfert nuclei are usually characterized by a H_2/Brγ ratio of the order of unity. The lowest of our values are the ones measured in the circumnuclear regions and agree with the expected values for pure starburst emission. On the other hand, the highest values are the ones measured in the nucleus of the galaxies, which are in the range usually occupied by LINER nuclei. While this is consistent with the nuclear classification of NGC 3627 and NGC 4536, the galaxy NGC 3351 is known to be a non-AGN. However, the high value of H_2/Brγ displayed by the nucleus of this galaxy can be explained as a consequence of the relative old stellar population that characterizes its innermost regions (see below), in which the presence young OB stars responsible for the Brγ emission has declined and the number of SN explosions, which heat the gas via shocks and produce the H_2 emission, has increased. Although a detailed interpretation of the variation of the H_2/Brγ from pure-starburst emission to Seyfert and LINER nuclei is non-trivial, one appealing scenario is that the different line ratios reflect different excitation mechanisms, in the sense that they describe a transition from purely ionizing radiation powered by star formation to pure shock excitation driven by SNRs. The H_2/Brγ derived for the galaxies together with the analysis of the excitation mechanisms presented in the previous section are compatible with this picture: the lowest H_2/Brγ ratios are displayed by the outer regions of NGC 4536, which are the ones with the strongest non-thermal contribution (UV fluorescence) to the excitation of the H_2 molecule, while the highest H_2/Brγ ratios are measured for regions with a strong influence from thermal processes (e.g. shock heating).

4.2.1 *Star-forming rings in NGC 3351 and NGC 4536*

The SINFONI data presented here allowed us to spatially resolve the innermost regions of NGC 3351 and NGC 4536, both of which show circumnuclear rings traced by ionized gas (i.e. Brγ and/or He I emission lines). This type of ring is frequently found in early to intermediate Hubble-type barred galaxies, and is usually associated with inflowing gas accumulating near the inner Lindblad resonances of bars (see Buta & Combes 1996 and references therein). Photoionization by OB stars is the most likely source of the nebular emission, although shocks produced by stellar winds and supernovae (SNe; related to the same stellar population) may play an additional role. In addition, high-energy photons from AGN can also ionize the interstellar medium and contribute to the Brγ emission. Although NGC 4536 is known to harbour a low-luminosity AGN, the spatial distribution of its Brγ emission (Fig. 6) indicates that this contribution is relatively low and restricted to the innermost regions, with no or negligible influence in the circumnuclear ring observed in this galaxy. Therefore, outside the nucleus we consider Brγ as a primary tracer of young stellar populations.

It is possible to estimate upper limits of the age of the star formation occurring in these galaxies by measuring the equivalent width of the Brγ line, $W_{Br\gamma}$. For this, we extracted two spectra for each galaxy, one integrating the emission of the inner ∼1 arcsec of the galaxies and a second one encompassing the emission coming from the ring. Note that in the case of NGC 3351 only part of the circumnuclear ring is covered by the FOV of our data (Section 3.1). We measured $W_{Br\gamma}$ of 0.3 and 2.1 Å for NGC 3351 and 0.8 and 8.3 Å for NGC 4536, with the higher values corresponding to the ring spectra. Using the Starburst99 models (Leitherer et al. 1999) for an instantaneous burst, different slopes for the initial mass function (IMF; 2.35 and 3.33), upper mass limits of 30 and 100 $M_\odot$ and solar metallicity, the measured values of $W_{Br\gamma}$ predict ages of the stellar populations of 10.5 and 6.9 Myr for NGC 3351 and 7.2 and 6.5 Myr for NGC 4536, with the younger populations located in the circumnuclear rings. As mentioned above, the age values correspond to upper limits, since we have not taken into account the possible contribution from the AGN and/or underlying (old) stellar population to the continuum. This additional component increases the continuum level, producing lower values of $W_{Br\gamma}$ than the true ones and, hence, larger ages than the expected for pure star-forming regions. An estimation of the contribution of the AGN to the continuum can be made based on the values derived for the equivalent width of the CO(2–0) absorption line at 2.29 μm, $W_{CO(2-0)}$, as proposed by Davies et al. (2007). These authors showed that the intrinsic $W_{CO(2-0)}$ of any stellar population is typically ∼12 Å (with an uncertainty of ±20 per cent), independent of the star formation history and age. Therefore, for a stellar continuum diluted by additional non-stellar emission, the fraction of the stellar light can be estimated by the ratio of the observed and intrinsic equivalent widths of the CO feature. In order to check for a possible AGN contribution to the continuum in NGC 4536 we measured the $W_{CO(2-0)}$ in the nuclear and ring spectra of this galaxy. The values are $W_{CO(2-0)} = (13.6 \pm 0.8)$ Å for the nuclear region and (14.0 ± 0.7) Å for the ring. These values are in the range derived by Davies et al. (2007), suggesting that the contribution from the AGN to the observed continuum in NGC 4536 is negligible.

Alternatively, we could assume a scenario where continuous star formation is taking place. In this case, the Starburst99 models predict ages of more than 60 Myr for the measured $W_{\mathrm{Br}\gamma}$. Such old ages are improbable, since the star formation would need to be sustained over long periods of time in very localized regions, in which turbulence and heating from SNe will disrupt the molecular clouds after ∼20–30 Myr, inhibiting further star formation (e.g. Blitz et al. 2007).

In addition to Brγ, the spectra of NGC 4536 also display He I 2.06 μm emission along the circumnuclear ring (Fig. 6). The ionization energy required to produce He I recombination lines is 24.6 eV, almost a factor of 2 higher than that of the hydrogen (13.6 eV). Therefore, He I emission lines are expected to arise in the vicinity of very hot massive stars (most massive OB stars) and AGNs, where enough high-energy photons are available to ionize the He I gas. Since the hottest stars will vanish fastest, the He I/Brγ emission-line ratio can give us a qualitative estimation of the relative ages of the young star clusters located along the circumnuclear ring observed in NGC 4536. We measured a value of He I/Br$\gamma \simeq 0.5$ along the entire ring, showing no significant variations and/or gradients. Hence, the young star clusters along the ring of this galaxy have the same ages, suggesting a scenario where the star formation started at the same time over the entire structure. It must be kept in mind that this is only a qualitative interpretation, since a detailed assessment of the He I/Brγ ratio is complicated by additional dependences such as the geometry of the ionized gas, its density, dust content and helium abundances (e.g. Shields 1993; Lumsden, Puxley & Hoare 2001).

5 NUCLEAR MASS INVENTORY

5.1 Warm molecular gas mass

The total mass of the warm molecular hydrogen, M_{warm}, can be derived from the observed flux of the H_2 1–0 S(1) 2.12 μm emission line. Assuming a temperature $T = 2000$ K, the H_2 1–0 S(1) transition probability $A_{\mathrm{S(1)}} = 3.47 \times 10^{-7}$ s^{-1} and a population fraction in the $(v, J) = (1, 3)$ level $f_{(1,3)} = 0.0122$, the relation between the warm molecular mass and the H_2 1–0 S(1) emission-line flux is given by

$$M_{\mathrm{warm}} \simeq 5.0875 \times 10^{13} \left(\frac{D}{\mathrm{Mpc}}\right)^2 \left(\frac{F_{1-0\,\mathrm{S(1)}}}{\mathrm{erg\ s^{-1}\ cm^{-2}}}\right) 10^{0.4\ A_{2.2}}, \quad (3)$$

where D is the distance to the galaxy and $A_{2.2}$ is the extinction at 2.2 μm (e.g. Scoville et al. 1982). Unfortunately, the data presented here do not allow us to determine the extinction affecting the inner regions of the galaxies in our sample and therefore it is only possible to determine a lower limit for M_{warm}, assuming a value of $A_{2.2} = 0$. Taking into account that the absorption at the K-band is only ≈10 per cent of that at visible wavelengths (Cardelli, Clayton & Mathis 1989), and a typical extinction $A_V \sim 1.2$ mag (Ho et al. 1997), correcting for internal extinction will not increase the derived masses by more than 12 per cent (or a factor of 2 for an extreme case of $A_V \sim 7.7$). Table 3 lists the integrated masses of warm molecular gas derived for the different regions of the sample galaxies studied. These cover a wide range of values, ranging from ∼9 $\mathrm{M}_\odot$ in the inner 75 pc of NGC 3351 up to ∼300 $\mathrm{M}_\odot$ in the inner 280 pc of NGC 4536.

5.2 Cold molecular gas mass

In principle, the H_2 1–0 S(1) 2.12 μm emission does not necessarily reflect the cold gas distribution, since it also depends on an external source of energy capable of exciting the H_2 ro-vibrational levels, such as UV photons from young OB stars, shocks driven by SNRs or by outflows or winds from the active nucleus (see Section 4.1). Historically, the favoured proxy for estimating the amount of cold H_2 gas has been CO emission. However, it has been suggested that an estimate of the total content of cold H_2 gas can be obtained from the H_2 2.12 μm line luminosity ($L_{1-0\,\mathrm{S(1)}}$). This method has the advantage of being able to probe the innermost regions of nearby objects with higher spatial resolution than CO observations. Müller Sánchez et al. (2006) derived a mean conversion factor of 4000 $\mathrm{M}_\odot/\mathrm{L}_\odot$ (with a standard deviation of a factor of ∼2) from the relation between the H_2 2.12 μm luminosity and the H_2 mass traced by CO luminosity in a sample of 16 luminous and ultraluminous IR galaxies.[2] Taking into account equation (3), these values yield cold-to-warm H_2 mass ratios in the range of $M_{\mathrm{cold}}/M_{\mathrm{warm}} \simeq (1\text{–}5) \times 10^6$. On the other hand, Dale et al. (2005) studied a large sample of active and star-forming galaxies and found cold-to-warm H_2 mass ratios covering a much larger range of values, $M_{\mathrm{cold}}/M_{\mathrm{warm}} \simeq 10^{5-7}$.

In order to investigate the relation between the H_2 2.12 μm emission and the cold H_2 mass, we compiled from the literature values of M_{cold} derived from CO observations and H_2 2.12 μm luminosities[3] for a large number of galaxies, covering a wide range of luminosities, morphological types and nuclear activity. Panel (a) of Fig. 10 shows the values of M_{cold} derived from CO observations as a function of the integrated area (i.e. size of the aperture used to integrate the CO flux). The relation between the cold H_2 gas mass and the integrated area, A, can be described as a power law $M_{\mathrm{cold}} = \alpha \mathrm{A}^\gamma$, with the best-fitting parameters $\alpha = (1.0 \pm 0.3) \times 10^6$ and $\gamma = 0.39 \pm 0.06$. Many factors contribute to the large dispersion observed in this relation [$\sigma(\log(\mathrm{M})) = 0.5$], including uncertainties in the CO-to-H_2 conversion factor (which likely differs from galaxy to galaxy), the inhomogeneity in the type of galaxies included and the intrinsic irregularity in the gas distribution of the galaxies (e.g. presence of bars, rings). Similarly, panel (b) of Fig. 10 shows the distribution, as a function of the integrated area, of the H_2 2.12 μm luminosities compiled from the literature. These follow a similar trend as the cold H_2 masses, with a value of $\gamma = 0.49 \pm 0.07$ consistent at 1σ with the one derived for the M_{cold} distribution. This is in agreement with the previous suggestion of a proportionality between the warm and cold molecular gas masses and gives us an opportunity to obtain a rough estimation of the factor relating these two quantities. Assuming that the two relations have the same slope ($\gamma = 0.39$), the proportionality factor can be estimated by minimizing the residuals of the rescaled luminosities, $\beta \times L_{1-0\,S(1)}$, with

[2] One outlier, NGC 6240, with a corresponding factor of only 400 $\mathrm{M}_\odot/\mathrm{L}_\odot$, was taken out of the sample.

[3] References for the CO data: Sakamoto et al. (1999b,a, 2011); Walter et al. (2001, 2002); Schinnerer et al. (2002); García-Burillo et al. (2003); Gao & Solomon (2004); Combes et al. (2004, 2009); Onodera et al. (2004); García-Barreto et al. (2005); Jogee et al. (2005); Boone et al. (2007); Iono et al. (2007); Hicks et al. (2009); Israel (2009); Zhu et al. (2009); Casasola et al. (2010, 2011); Martín et al. (2010); Meier et al. (2010); Olsson et al. (2007, 2010); Alatalo et al. (2011); Crocker et al. (2011); Salomé et al. (2011). References for H_2 2.12 μm line luminosities: Dale et al. (2004); Rodríguez-Ardila et al. (2004); Davies et al. (2006); Müller Sánchez et al. (2006); Zuther et al. (2007); Büker et al. (2008); Nowak et al. (2008); Riffel et al. (2008, 2010); Hicks et al. (2009); Storchi-Bergmann et al. (2009); Friedrich et al. (2010).

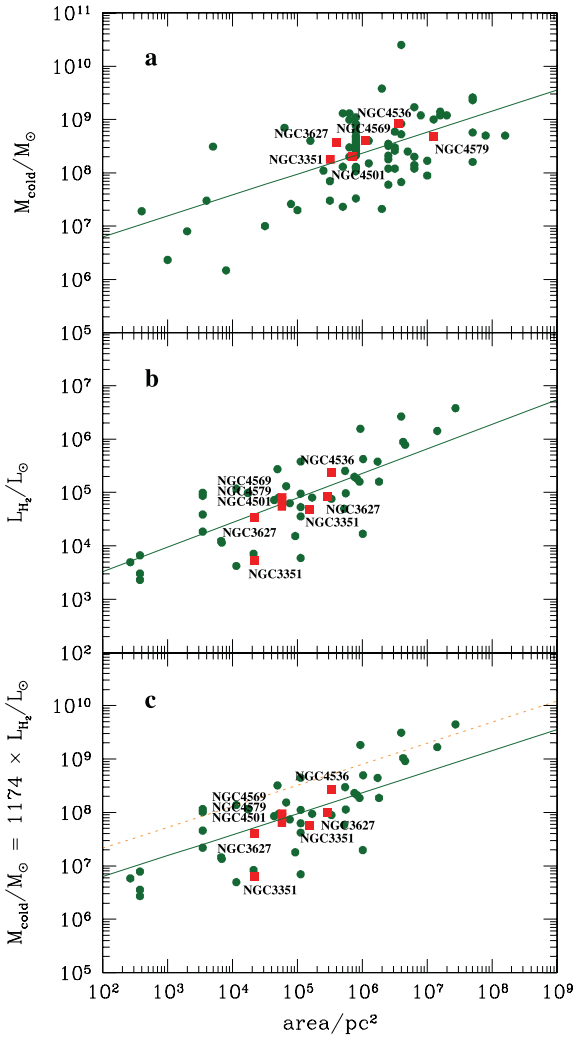

Figure 10. Panel (a): cold H_2 gas masses derived from CO observations as a function of the integrated area. The solid line corresponds to the power law that best reproduces the data. Panel (b): H_2 2.12 μm luminosities as a function of the integrated area. The solid line corresponds to a power-law fit to these data. Panel (c): cold H_2 gas masses derived from H_2 2.12 μm luminosities using a rescaling factor $\beta = 1174\,M_\odot/\,L_\odot$. The solid line corresponds to the same power law as in panel (a), while the dashed line corresponds to the relation that would be obtained using a factor of $\beta = 4000\,M_\odot/\,L_\odot$ (see the text for details). The red squares correspond to values of the galaxies in our sample.

respect to the power law that best describes the distribution of cold H_2 masses derived from the CO measurements. Panel (c) of Fig. 10 shows the values of L_{H_2} compiled from the literature rescaled by the factor $\beta = 1174\,M_\odot/\,L_\odot$ obtained in this way. We also included the result obtained using the rescaling factor of $4000\,M_\odot/\,L_\odot$ proposed by Müller Sánchez et al. (2006) (dashed line). Note that if we had used that factor, we would had overestimated the masses as compared to the ones derived from the CO observations. Therefore, the factor of 1174 seems to give more representative cold H_2 masses for a larger range of galaxy types. This factor and its corresponding error ($\sigma \log(\beta) = 0.35$) can be translated to a range of M_{cold}/M_{warm} ratio of $\simeq (0.3-1.6) \times 10^6$, which is consistent with the one derived by Dale et al. (2005) and marginally consistent with the one inferred by Müller Sánchez et al. (2006).

From the analysis described above, we can conclude that a rough estimate of the cold H_2 gas mass can be obtained from the integrated H_2 2.12 μm luminosity using the relation

$$\frac{M_{cold}}{M_\odot} \approx 1174 \times \frac{L_{1-0\,S(1)}}{L_\odot}. \quad (4)$$

Taking this relation into account, we calculated the total (cold) H_2 gas content for the galaxies in our sample. The observed H_2 2.12 μm line fluxes and corresponding cold H_2 masses of the nuclear and circumnuclear regions of the sample galaxies are listed in Table 3. We found masses between 4×10^5 and $2.7 \times 10^8\,M_\odot$ within regions with radii of up to 280 pc. In order to place these results within a larger context, we included in the lower panel of Fig. 10 the cold H_2 masses derived from the H_2 2.12 μm luminosities measured for the largest regions in each galaxy. The masses obtained for these galaxies agree very well with the 'global' trend followed by the large pool of masses taken from the literature. The only galaxy that seems to deviate from this trend is NGC 3351, for which the inner regions show a lower cold-to-warm mass ratio than the rest of the sample. However, this ratio goes up when it is calculated within a larger radius region (i.e. 8×8 arcsec^2).

The values of M_{cold} derived from the H_2 luminosities can be compared with values derived from CO observations. For this, we also included in the upper panel of Fig. 10 values of M_{cold} derived from CO observations for the galaxies in our sample [NGC 3351: Devereux et al. (1992); NGC 3627: Regan et al. (2002); NGC 4501: Onodera et al. (2004); NGC 4536: Jogee et al. (2005); NGC 4569: Boone et al. (2007); NGC 4579: García-Burillo et al. (2009)]. Taking into account the different sizes of the regions probed by the H_2 2.12 μm and CO observations, we can conclude that both measurements yield consistent results.

5.3 Stellar and gas mass distributions and its implications for the M_{BH} estimation

Modelling the dynamics of stars in galactic nuclei is one of the preferred methods to probe the central potential of inactive galaxies and directly determine the mass of the central BH. However, in dynamical modelling, the *total* enclosed mass is constrained, including not only stars and the putative central BH, but also other components that could be present in the nucleus, such as dark matter (DM) and gas. The estimation of the relative importance of these components is essential, since it will be reflected in the derived mass-to-light ratio (M/L ratio) and M_{BH}. The need for including a DM halo in the dynamical modelling has been the focus of a number of recent publications (e.g. Gebhardt & Thomas 2009; Shen & Gebhardt 2010; Gebhardt et al. 2011; Jardel et al. 2011; McConnell et al. 2011b, 2012; Schulze & Gebhardt 2011; Rusli et al. 2012a). It becomes an issue if the sphere of influence of the BH is not well resolved (Rusli et al. 2012a). The omission of a separate DM component forces the DM to be incorporated into the supposed 'stellar' mass. Hence, the stellar M/L ratio increases. Since M/L ratio is assumed to be radially constant, this results in an overestimation of the central 'stellar' mass that, in turn, is compensated by a lower M_{BH}. Significant amount of gas could affect the measured M_{BH} similarly. If the gas adds mass outside the BH's sphere of influence, its omission could, in analogy to DM, force again a higher M/L ratio and low M_{BH}. If instead, the gas is concentrated near the BH, its mass could go directly in the M_{BH}, biasing it too high. Here, we will address the question of how much the presence of gas could affect the dynamical M_{BH} measurements.

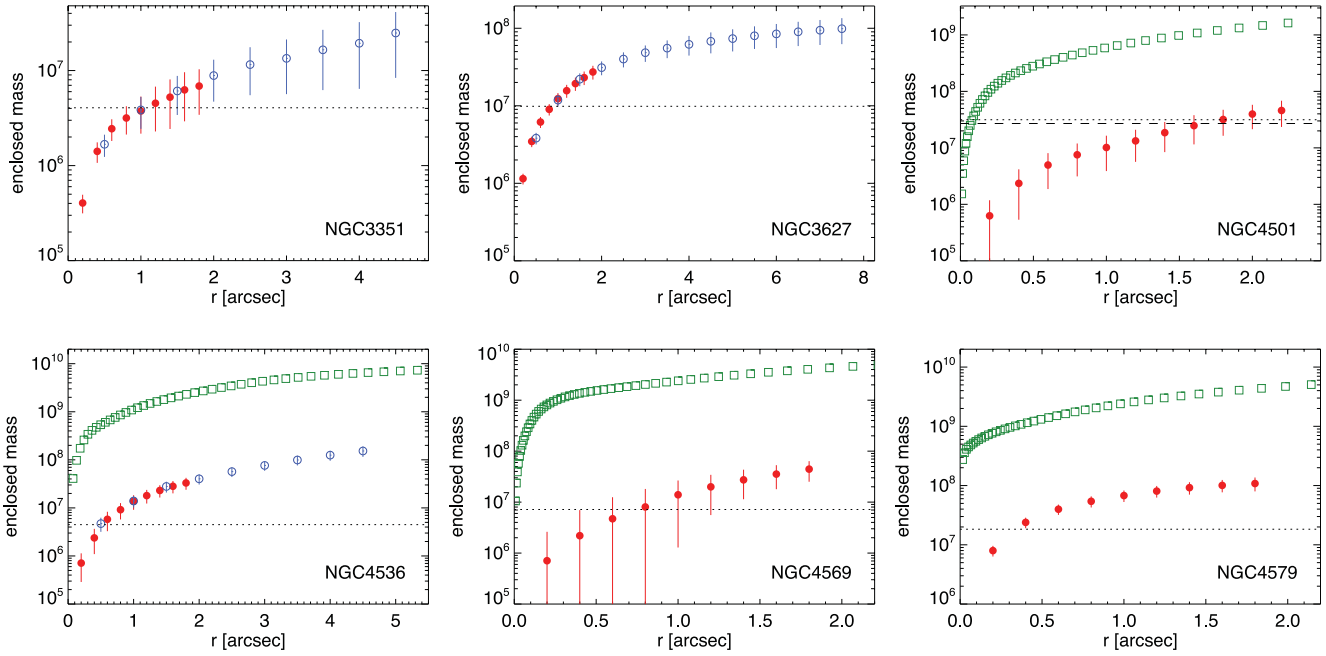

Figure 11. Deprojected enclosed molecular and stellar masses measured inside a given radius for the galaxies in the sample. The blue open circles and the red filled circles correspond to the molecular mass measured from the low-resolution and high-resolution data cubes, respectively. The green squares indicate the enclosed stellar mass distribution derived for NGC 4501, NGC 4536 and NGC 4569. The error bars reflect the 3σ uncertainties in the H_2 emission-line flux measurements. The dotted line in each panel indicates the M_{BH} of the galaxy derived from its sigma (Table 4) and the dashed line in the upper-right panel indicates the values of the M_{BH} of NGC 4501 derived from the dynamical modelling.

In the previous section, we showed that it is possible to estimate the mass of the molecular gas from the H_2 2.12 μm emission-line flux. We used this result to derive the deprojected gas masses enclosed within a given radius for the galaxies in the sample. For this, we assumed that the gas is contained in a thin disc located in the plane of the galaxy and measured the H_2 emission-line flux in spectra extracted from the continuum-subtracted cubes using elliptical apertures. The size and shape of the apertures were determined by the inclination angle and semimajor axis of the corresponding galaxy (Table 2), in a way that corresponds to circular apertures on the plane of the disc/galaxy. Fig. 11 shows the deprojected enclosed masses as a function of the radius measured for the galaxies in the sample. The molecular gas masses measured inside the smallest aperture, $r = 0.2$ arcsec (or 10–16 pc), vary between 4×10^5 and 8×10^7 $M_\odot$, and reach $\sim 10^8$ $M_\odot$ inside larger apertures. Particularly noticeable is the relatively high gas mass content of the galaxy NGC 4579, which shows the highest measured mass value of the whole sample inside a region of just a few arcsec (i.e. $r = 2$ arcsec). Although this value is slightly higher than the one derived for the 3×3 arcsec^2 region of this galaxy (see Table 3), these measurements are consistent within the errors. The difference is due to the different approaches followed in the determination of the continuum of the spectrum in each region.

The ranges of gas masses found in the nucleus of the galaxies in our sample are comparable to the range of M_{BH} usually found in the centre of galaxies. From the stellar velocity dispersion σ and the rotational velocity V profiles available in the literature, it is possible to estimate the M_{BH} of the galaxies using the $M_{BH}-\sigma_e$ (as in Gültekin et al. 2009). Table 4 lists the values of $\sigma_e = (\sigma^2 + V^2)^{1/2}$ derived for the galaxies in our sample and the corresponding M_{BH} assuming the $M_{BH}-\sigma$ relation given by McConnell et al. (2011a) for spiral galaxies. The estimated M_{BH} are about an order of magnitude higher than the mass of the gas contained inside a region of $r =$ 0.2 arcsec for all the galaxies except NGC 4579 (see Fig. 11). As we mentioned above, the latter shows a particularly high content of gas. The galaxy NGC 4501 harbours the largest BH mass from the all sample, which is consistent with the value $M_{BH} = 2.7 \times 10^7$ $M_\odot$ obtained from the dynamical modelling of the stars following the method described by Nowak et al. (2007), which is based on the Schwarzschild superposition code of Thomas et al. (2004). The full analysis of the stellar dynamical modelling of NGC 4501 will be presented in Erwin et al. (in preparation).

Table 4. Estimated BH masses for the galaxies in the sample.

Galaxy	$(\sigma^2 + V^2)^{1/2}$ (km s^{-1})	M_{BH}[a] (10^6 $M_\odot$)
NGC 3351	100.9 ± 9.1	4.0 (2.6–6.0)
NGC 3627	122.4 ± 7.3	9.8 (7.4–12.8)
NGC 4501	157.8 ± 36.9	31.5 (92.9–82.6)
NGC 4536	103.1 ± 14.5	4.5 (2.2–8.2)
NGC 4569	114.2 ± 13.6	7.2 (4.0–12.0)
NGC 4579	140.2 ± 16.0	18.3 (10.5–30.1)

[a]The numbers between parentheses correspond to the lower and upper limits of the M_{BH} given by the errors in sigma.

But how large is the gas mass in comparison to the stellar mass, and how much can it affect the M_{BH} dynamical estimates? To answer this question we have included in Fig. 11 the deprojected spherical stellar masses as a function of the radius for the galaxies NGC 4501, NGC 4536, NGC 4569 and NGC 4579. These distributions were obtained from the luminosity profile and the M/L ratio derived for each galaxy. The luminosity density profiles were obtained by deprojecting surface-brightness profiles using a modified version of the algorithm of Magorrian (1999), taking into account the effects

of PSF convolution (see Rusli et al. 2011). The surface-brightness profiles (typically in near-IR bands such as *H* and *K*) were derived from a combination of ellipse fits to isophotes and 2D modelling of images, using high-resolution *HST* images for the smallest scales and SDSS or *Spitzer* IRAC images for larger scales; in cases where only optical *HST* images were available and strong near-nuclear dust lanes were present, we also used *K*-band images derived from our SINFONI data cubes. Details for individual galaxies, along with the dynamical modelling, will be discussed in Erwin et al. (in preparation). In the case of NGC 4501, the M/L ratio was obtained from stellar dynamical modelling. For the other galaxies (NGC 4536, NGC 4569 and NGC 4579, for which dynamical modelling is not yet complete), we derived the M/L ratio from the colours of the galaxies and the transformations given by Zibetti, Charlot & Rix (2009) and Bell & de Jong (2001). These M/L are based on scaled Salpeter and Chabrier IMFs for Bell & de Jong (2001) and Zibetti et al. (2009), respectively. Recently, evidence for a more dwarf-dominated IMF in hot stellar systems has grown (e.g. Thomas et al. 2011; Cappellari et al. 2012; Conroy & van Dokkum 2012; Dutton et al. 2012). Hence, our M/L should be considered as lower limits for the actual stellar masses. From the analysis of the inner 5 arcsec of the galaxies in WFPC2 archive images, we derived average colours of $B - V = 1.0$ for NGC 4536, $V - I = 1.2$ for NGC 4569 and $V - I = 1.3$ for NGC 4579. These values are in very good agreement with the ones reported in the photometric compilation of Prugniel & Heraudeau (1998) for the smallest (∼6.6 arcsec) aperture, and correspond to $M/L_K = 0.6$, $M/L_H = 1.2$ and $M/L_K = 1.0$ for NGC 4536, NGC 4569 and NGC 4579, respectively.

It is clear from Fig. 11 that the gas content of these galaxies is negligible compared to the stellar mass, which exceeds the former by more than an order of magnitude. In all the galaxies, the gas mass is no more than 0.1–3 per cent of the stellar mass, and even though the galaxies have considerable amounts of gas present in their nuclei, it is not enough to affect the dynamical $M_{\rm BH}$ measurements based only on the observed stellar features of the galaxy.

6 SUMMARY AND CONCLUSIONS

We have presented new AO-assisted *K*-band SINFONI/VLT IFS observations of a sample of six nearby galaxies, NGC 3351, NGC 3627, NGC 4501, NGC 4536, NGC 4569 and NGC 4579. This is the first of two companion papers analysing the gas properties of these galaxies, and is part of a series reporting the results of our SINFONI survey aimed at expanding the number of reliable BH masses in the nucleus of galaxies by means of dynamical modelling.

The SINFONI spectra of the galaxies in the sample display several H_2 emission lines and, in some cases, ionized hydrogen and helium emission lines. This, together with the high spatial resolution provided by the observations, allowed us to study in detail the morphology and physical properties of the emission-line gas located in the innermost regions of the galaxies, and the star-forming regions associated with it. Additionally, we have derived the gas mass content of the galaxies and compared it with their stellar masses in order to check if it could affect the BH masses derived from stellar dynamical modelling. Our main results are summarized below.

(i) A rich diversity of morphologies is seen in the H_2 emission-line gas distributions of galaxies, including bar- and ring-like structures, centrally concentrated emission and off-centre irregular distributions. When detected, the emission lines from ionized gas (i.e. Brγ and He I) showed also a variety of morphologies, not necessarily coincident with the H_2 emission-line distribution.

(ii) H_2 emission-line ratios point towards thermal processes as the main mechanism responsible for the excitation of the H_2 emission-line gas, independent of the type of nuclear activity of the galaxies. However, non-thermal processes are not completely ruled out, and seem to have a relative stronger contribution in the regions closer to AGNs. This scenario is supported by the measured H_2/Brγ ratios, which are higher in the nuclear regions of the galaxies.

(iii) The high spatial resolution provided by the SINFONI data allowed us to resolve the circumnuclear rings traced by ionized gas in the central regions of NGC 3351 and NGC 4536. The analysis of the Brγ equivalent width indicates that the star formation in the ring of NGC 3351 and NGC 4536 started 6.9 and 6.5 Myr ago, respectively. Additionally, the He I/Brγ emission-line ratio measured in NGC 4536 is approximately constant, suggesting that the star formation started at the same time along the entire ring.

(iv) We found that a rescaling of the H_2 2.12 μm emission-line luminosity by a factor $\beta \simeq 1200$ gives a good estimate (within a factor of 2) of the total (cold) molecular gas mass.

(v) The galaxies in the sample contain large quantities of molecular gas, with total masses in the range $\sim 10^5$–10^8 $M_\odot$. Nevertheless, these masses are only a 3 per cent (at most) of the corresponding stellar masses. Hence, BH mass estimates based on the dynamical modelling of the stars should not be affected by the presence of gas.

ACKNOWLEDGMENTS

We thank the referee for his/her constructive comments on our manuscript. We also thank the Paranal Observatory Team for support during the observations. SPR acknowledges support from the DFG Cluster of Excellence 'Origin and Structure of the Universe'. PE was supported by the Deutsche Forschungsgemeinschaft through the Priority Programme 1177 'Galaxy Evolution'. This research has made use of the NASA/IPAC Infrared Science Archive (IRSA) and the NASA/IPAC Extragalactic Database (NED), which are operated by the Jet Propulsion Laboratory, California Institute of Technology, under contract with the National Aeronautics and Space Administration.

REFERENCES

Abuter R., Schreiber J., Eisenhauer F., Ott T., Horrobin M., Gillesen S., 2006, New Astron. Rev., 50, 398
Alatalo K. et al., 2011, ApJ, 735, 88
Alonso-Herrero A., Rieke M. J., Rieke G. H., Shields J. C., 2000, ApJ, 530, 688
Barth A. J., Shields J. C., 2000, PASP, 112, 753
Bell E. F., de Jong R. S., 2001, ApJ, 550, 212
Black J. H., van Dishoeck E. F., 1987, ApJ, 322, 412
Blitz L., Fukui Y., Kawamura A., Leroy A., Mizuno N., Rosolowsky E., 2007, in Reipurth B., Jewitt D., Keil K., eds, Protostars and Planets V. Univ. Arizona Press, Tucson, AZ, p. 81
Böker T., Falcón-Barroso J., Schinnerer E., Knapen J. H., Ryder S., 2008, AJ, 135, 479
Bonnet H. et al., 2004, The Messenger, 117, 17
Boone F. et al., 2007, A&A, 471, 113
Boone F. et al., 2011, A&A, 525, A18
Brand P. W. J. L., Toner M. P., Geballe T. R., Webster A. S., Williams P. M., Burton M. G., 1989, MNRAS, 236, 929
Buta R., Combes F., 1996, Fundam. Cosm. Phys., 17, 95
Buta R. J. et al., 2010, ApJS, 190, 147
Cappellari M., Copin Y., 2003, MNRAS, 342, 345
Cappellari M., Emsellem E., 2004, PASP, 116, 138
Cappellari M. et al., 2012, Nat, 484, 485
Cardelli J. A., Clayton G. C., Mathis J. S., 1989, ApJ, 345, 245

Carollo C. M., Stiavelli M., Mack J., 1998, AJ, 116, 68
Casasola V., Hunt L. K., Combes F., García-Burillo S., Boone F., Eckart A., Neri R., Schinnerer E., 2010, A&A, 510, A52
Casasola V., Hunt L. K., Combes F., García-Burillo S., Neri R., 2011, A&A, 527, A92
Cayatte V., Kotanyi C., Balkowski C., van Gorkom J. H., 1994, AJ, 107, 1003
Colina L., Garcia Vargas M. L., Mas-Hesse J. M., Alberdi A., Krabbe A., 1997, ApJ, 484, L41
Combes F. et al., 2004, A&A, 414, 857
Combes F. et al., 2009, A&A, 503, 73
Conroy C., van Dokkum P., 2012, prepint (arXiv:1205.6473)
Crocker A. F., Bureau M., Young L. M., Combes F., 2011, MNRAS, 410, 1197
Dale D. A. et al., 2004, ApJ, 601, 813
Dale D. A., Sheth K., Helou G., Regan M. W., Hüttemeister S., 2005, AJ, 129, 2197
Davies R. I., 2007, MNRAS, 375, 1099
Davies R. I., Sugai H., Ward M. J., 1997, MNRAS, 291, 314
Davies R. I., Sternberg A., Lehnert M. D., Tacconi-Garman L. E., 2005, ApJ, 633, 105
Davies R. I. et al., 2006, ApJ, 646, 754
Davies R. I., Müller Sánchez F., Genzel R., Tacconi L. J., Hicks E. K. S., Friedrich S., Sternberg A., 2007, ApJ, 671, 1388
de Vaucouleurs G., de Vaucouleurs A., Corwin J. H. G., Buta R. J., Paturel G., Fouqué P., 1991, Third Reference Catalogue of Bright Galaxies. Volume I: Explanations and references. Volume II: Data for galaxies between 0^h and 12^h. Volume III: Data for galaxies between 12^h and 24^h. Springer, New York
Devereux N. A., Kenney J. D., Young J. S., 1992, AJ, 103, 784
Dors J. O. L., Riffel R. A., Cardaci M. V., Hägele G. F., Krabbe Á. C., Pérez-Montero E., Rodrigues I., 2012, MNRAS, 422, 252
Draine B. T., Woods D. T., 1990, ApJ, 363, 464
Dutton A. A. et al., 2012, MNRAS, accepted, prepint (arXiv:1206.4310)
Eisenhauer F. et al., 2003, Proc. SPIE, 4841, 1548
Elmegreen D. M., Elmegreen B. G., 1987, ApJ, 314, 3
Elmegreen D. M., Chromey F. R., Bissell B. A., Corrado K., 1999, AJ, 118, 2618
Englmaier P., Shlosman I., 2000, ApJ, 528, 677
Erwin P., 2005, MNRAS, 364, 283
Ferland G. J., Korista K. T., Verner D. A., Ferguson J. W., Kingdon J. B., Verner E. M., 1998, PASP, 110, 761
Ferrarese L., Merritt D., 2000, ApJ, 539, L9
Filho M. E., Barthel P. D., Ho L. C., 2000, ApJS, 129, 93
Freedman W. L. et al., 2001, ApJ, 553, 47
Friedrich S., Davies R. I., Hicks E. K. S., Engel H., Müller-Sánchez F., Genzel R., Tacconi L. J., 2010, A&A, 519, A79
Gabel J. R., Bruhweiler F. C., 2002, AJ, 124, 737
Gao Y., Solomon P. M., 2004, ApJS, 152, 63
García-Barreto J. A., Scoville N. Z., Koda J., Sheth K., 2005, AJ, 129, 125
García-Burillo S. et al., 2003, A&A, 407, 485
García-Burillo S., Combes F., Schinnerer E., Boone F., Hunt L. K., 2005, A&A, 441, 1011
García-Burillo S. et al., 2009, A&A, 496, 85
Gebhardt K., Thomas J., 2009, ApJ, 700, 1690
Gebhardt K. et al., 2000, ApJ, 539, L13
Gebhardt K., Adams J., Richstone D., Lauer T. R., Faber S. M., Gültekin K., Murphy J., Tremaine S., 2011, ApJ, 729, 119
Gredel R., Dalgarno A., 1995, ApJ, 446, 852
Gültekin K. et al., 2009, ApJ, 698, 198
Häring N., Rix H.-W., 2004, ApJ, 604, L89
Helfer T. T., Thornley M. D., Regan M. W., Wong T., Sheth K., Vogel S. N., Blitz L., Bock D. C.-J., 2003, ApJS, 145, 259
Hicks E. K. S., Davies R. I., Malkan M. A., Genzel R., Tacconi L. J., Müller Sánchez F., Sternberg A., 2009, ApJ, 696, 448
Ho L. C., Filippenko A. V., Sargent W. L. W., 1997, ApJS, 112, 315
Ho L. C. et al., 2001, ApJ, 549, L51
Iono D. et al., 2007, ApJ, 659, 283
Israel F. P., 2009, A&A, 506, 689
Jardel J. R. et al., 2011, ApJ, 739, 21
Jogee S., 2006, in Alloin D., Johnson R., Lira P., eds, Lecture Notes in Physics, Vol. 693, Physics of Active Galactic Nuclei at all Scales. Springer, Berlin and Heidelberg, p. 143
Jogee S., Scoville N., Kenney J. D. P., 2005, ApJ, 630, 837
Keel W. C., 1996, PASP, 108, 917
Kenney J. D., Young J. S., 1986, ApJ, 301, L13
Knapen J. H., Pérez-Ramírez D., Laine S., 2002, MNRAS, 337, 808
Knapen J. H., de Jong R. S., Stedman S., Bramich D. M., 2003, MNRAS, 344, 527
Koopmann R. A., Kenney J. D. P., 2004, ApJ, 613, 866
Kormendy J., Richstone D., 1995, ARA&A, 33, 581
Laine S., Kotilainen J. K., Reunanen J., Ryder S. D., Beck R., 2006, AJ, 131, 701
Larkin J. E., Armus L., Knop R. A., Soifer B. T., Matthews K., 1998, ApJS, 114, 59
Leitherer C. et al., 1999, ApJS, 123, 3
Lepp S., McCray R., 1983, ApJ, 269, 560
Lumsden S. L., Puxley P. J., Hoare M. G., 2001, MNRAS, 320, 83
Maciejewski W., 2004a, MNRAS, 354, 883
Maciejewski W., 2004b, MNRAS, 354, 892
Magorrian J., 1999, MNRAS, 302, 530
Magorrian J. et al., 1998, AJ, 115, 2285
Maloney P. R., Hollenbach D. J., Tielens A. G. G. M., 1996, ApJ, 466, 561
Maoz D., Filippenko A. V., Ho L. C., Rix H.-W., Bahcall J. N., Schneider D. P., Macchetto F. D., 1995, ApJ, 440, 91
Maoz D., Koratkar A., Shields J. C., Ho L. C., Filippenko A. V., Sternberg A., 1998, AJ, 116, 55
Marconi A., Hunt L. K., 2003, ApJ, 589, L21
Martín S., George M. R., Wilner D. J., Espada D., 2010, AJ, 139, 2241
Martini P., Regan M. W., Mulchaey J. S., Pogge R. W., 2003, ApJS, 146, 353
McAlpine W., Satyapal S., Gliozzi M., Cheung C. C., Sambruna R. M., Eracleous M., 2011, ApJ, 728, 25
McConnell N. J., Ma C.-P., Gebhardt K., Wright S. A., Murphy J. D., Lauer T. R., Graham J. R., Richstone D. O., 2011a, Nat, 480, 215
McConnell N. J., Ma C.-P., Graham J. R., Gebhardt K., Lauer T. R., Wright S. A., Richstone D. O., 2011b, ApJ, 728, 100
McConnell N. J., Ma C.-P., Murphy J. D., Gebhardt K., Lauer T. R., Graham J. R., Wright S. A., Richstone D. O., 2012, ApJ, 756, 179
Mei S. et al., 2007, ApJ, 655, 144
Meier D. S., Turner J. L., Beck S. C., Gorjian V., Tsai C.-W., Van Dyk S. D., 2010, AJ, 140, 1294
Modigliani A. et al., 2007, preprint (arXiv:astro-ph/0701297)
Moorwood A. F. M., Oliva E., 1988, A&A, 203, 278
Moorwood A. F. M., Oliva E., 1990, A&A, 239, 78
Mouri H., 1994, ApJ, 427, 777
Müller Sánchez F., Davies R. I., Eisenhauer F., Tacconi L. J., Genzel R., Sternberg A., 2006, A&A, 454, 481
Nakanishi H., Sofue Y., Koda J., 2005, PASJ, 57, 905
Nowak N., Saglia R. P., Thomas J., Bender R., Pannella M., Gebhardt K., Davies R. I., 2007, MNRAS, 379, 909
Nowak N., Saglia R. P., Thomas J., Bender R., Davies R. I., Gebhardt K., 2008, MNRAS, 391, 1629
Nowak N., Thomas J., Erwin P., Saglia R. P., Bender R., Davies R. I., 2010, MNRAS, 403, 646
Olsson E., Aalto S., Thomasson M., Beswick R., Hüttemeister S., 2007, A&A, 473, 389
Olsson E., Aalto S., Thomasson M., Beswick R., 2010, A&A, 513, A11
Onodera S., Koda J., Sofue Y., Kohno K., 2004, PASJ, 56, 439
Planesas P., Colina L., Perez-Olea D., 1997, A&A, 325, 81
Pogge R. W., 1989, ApJS, 71, 433
Pogge R. W., De Robertis M. M., 1993, ApJ, 404, 563
Pogge R. W., Maoz D., Ho L. C., Eracleous M., 2000, ApJ, 532, 323
Pompea S. M., Rieke G. H., 1990, ApJ, 356, 416
Prugniel P., Heraudeau P., 1998, A&AS, 128, 299
Puxley P. J., Hawarden T. G., Mountain C. M., 1988, MNRAS, 231, 465

Quillen A. C., Alonso-Herrero A., Rieke M. J., McDonald C., Falcke H., Rieke G. H., 1999, ApJ, 525, 685
Rabien S., Davies R. I., Ott T., Li J., Abuter R., Kellner S., Neumann U., 2004, Proc. SPIE, 5490, 981
Regan M. W., Thornley M. D., Helfer T. T., Sheth K., Wong T., Vogel S. N., Blitz L., Bock D. C.-J., 2001, ApJ, 561, 218
Regan M. W., Sheth K., Teuben P. J., Vogel S. N., 2002, ApJ, 574, 126
Reunanen J., Kotilainen J. K., Prieto M. A., 2002, MNRAS, 331, 154
Rhee J. H., Larkin J. E., 2005, ApJ, 620, 151
Riffel R. A., Storchi-Bergmann T., Winge C., Barbosa F. K. B., 2006, MNRAS, 373, 2
Riffel R. A., Storchi-Bergmann T., Winge C., McGregor P. J., Beck T., Schmitt H., 2008, MNRAS, 385, 1129
Riffel R. A., Storchi-Bergmann T., Nagar N. M., 2010, MNRAS, 404, 166
Rodríguez-Ardila A., Pastoriza M. G., Viegas S., Sigut T. A. A., Pradhan A. K., 2004, A&A, 425, 457
Rodríguez-Ardila A., Riffel R., Pastoriza M. G., 2005, MNRAS, 364, 1041
Rosenberg M. J. F., van der Werf P. P., Israel F. P., 2012, A&A, 540, A116
Rubin V. C., Peterson C. J., Ford J. W. K., 1975, ApJ, 199, 39
Rusli S. P., Thomas J., Erwin P., Saglia R. P., Nowak N., Bender R., 2011, MNRAS, 410, 1223
Rusli S. et al., 2012a, AJ, submitted
Rusli S. P., Erwin P., Saglia R. P., Thomas J., Fabricius M., Bender R., Nowak N., 2012b, AJ, submitted
Sakamoto K., Okumura S. K., Ishizuki S., Scoville N. Z., 1999a, ApJ, 525, 691
Sakamoto K., Okumura S. K., Ishizuki S., Scoville N. Z., 1999b, ApJS, 124, 403
Sakamoto K., Mao R.-Q., Matsushita S., Peck A. B., Sawada T., Wiedner M. C., 2011, ApJ, 735, 19
Salomé P., Combes F., Revaz Y., Downes D., Edge A. C., Fabian A. C., 2011, A&A, 531, A85
Satyapal S., Vega D., Dudik R. P., Abel N. P., Heckman T., 2008, ApJ, 677, 926
Schinnerer E., Maciejewski W., Scoville N., Moustakas L. A., 2002, ApJ, 575, 826
Schreiber J., Thatte N., Eisenhauer F., Tecza M., Abuter R., Horrobin M., 2004, in Ochsenbein F., Allen M. G., Egret D., eds, ASP Conf. Ser. Vol. 314, Astronomical Data Analysis Software and Systems (ADASS) XIII. Astron. Soc. Pac., San Francisco, p. 380
Schulze A., Gebhardt K., 2011, ApJ, 729, 21
Scoville N. Z., Hall D. N. B., Ridgway S. T., Kleinmann S. G., 1982, ApJ, 253, 136
Shaw M., Axon D., Probst R., Gatley I., 1995, MNRAS, 274, 369
Shaw G., Ferland G. J., Abel N. P., Stancil P. C., van Hoof P. A. M., 2005, ApJ, 624, 794
Shen J., Gebhardt K., 2010, ApJ, 711, 484
Sheth K., Vogel S. N., Regan M. W., Teuben P. J., Harris A. I., Thornley M. D., 2002, AJ, 124, 2581
Shields J. C., 1993, ApJ, 419, 181
Shlosman I., Frank J., Begelman M. C., 1989, Nat, 338, 45
Sofue Y., Koda J., Nakanishi H., Onodera S., Kohno K., Tomita A., Okumura S. K., 2003, PASJ, 55, 17
Sternberg A., Dalgarno A., 1989, ApJ, 338, 197
Storchi-Bergmann T., McGregor P. J., Riffel R. A., Simões Lopes R., Beck T., Dopita M., 2009, MNRAS, 394, 1148
Telesco C. M., Dressel L. L., Wolstencroft R. D., 1993, ApJ, 414, 120
Thomas J., Saglia R. P., Bender R., Thomas D., Gebhardt K., Magorrian J., Richstone D., 2004, MNRAS, 353, 391
Thomas J. et al., 2011, MNRAS, 415, 545
Tremaine S. et al., 2002, ApJ, 574, 740
Turner J., Kirby-Docken K., Dalgarno A., 1977, ApJS, 35, 281
van den Bergh S., 1976, ApJ, 206, 883
Veilleux S., Goodrich R. W., Hill G. J., 1997, ApJ, 477, 631
Vila M. B., Pedlar A., Davies R. D., Hummel E., Axon D. J., 1990, MNRAS, 242, 379
Walter F., Taylor C. L., Hüttemeister S., Scoville N., McIntyre V., 2001, AJ, 121, 727
Walter F., Weiss A., Martin C., Scoville N., 2002, AJ, 123, 225
Wilson C. D. et al., 2009, ApJ, 693, 1736
Zhu M., Papadopoulos P. P., Xilouris E. M., Kuno N., Lisenfeld U., 2009, ApJ, 706, 941
Zibetti S., Charlot S., Rix H.-W., 2009, MNRAS, 400, 1181
Zuther J., Iserlohe C., Pott J.-U., Bertram T., Fischer S., Voges W., Hasinger G., Eckart A., 2007, A&A, 466, 451

APPENDIX A

In this section, we specify the location of the spatial regions from where we extracted the 1D spectra analysed in Section 4. The 1D spectra were obtained by summing up the signal inside elliptical apertures or the entire FOV (e.g. $\sim 3 \times 3$ arcsec^2 for the HR data). Table A1 lists the centre, sizes of the semimajor and -minor axis and PA of the elliptical apertures. The PA is defined as the angle between the positive x-axis of the data cube and the semimajor axis of the region (measured anticlockwise). The spectrum of the regions called 'Ring' of NGC 4501 and NGC 4536 corresponds to the region between two ellipses. In these cases we report the minimum and maximum semimajor and -minor axis. For the region '5 – Ring' of NGC 3351 we summed up the signal of the entire FOV outside the elliptical aperture specified in Table A1.

Table A1. Position and shape of the elliptical apertures used to extract the 1D spectra analysed in Section 4.

Galaxy regions	Centre (arcsec, arcsec)	Semimajor axis (arcsec)	Seminor axis (arcsec)	PA
NGC 3351				
1 – Nucleus	(0, 0)	0.75	0.55	90°
2 – W cloud	(1.05, −0.15)	0.3	0.3	0°
5 – Ring	(0, 0)	1.15−	1.15−	0°
NGC 3627				
1 – Nucleus	(0, 0)	1.0	0.75	90°
3 – N cloud	(− 3, 5.6)	0.87	0.87	0°
4 – S cloud	(2.1, −3.75)	0.87	0.87	0°
NGC 4501				
1 – Nucleus	(0.2, 0)	0.85	0.6	45°
2 – Ring	(0.2, 0)	0.85−2.25	0.6−1.9	45°
NGC 4536				
1 – Nucleus	(0, 0)	1.05	0.7	135°
2 – Ring	(0.25, −0.125)	1.875−5.375	0.5−1.25	90°
NGC 4579				
1 – Nucleus	(− 0.15, −0.1)	0.8	0.7	135°
2 – NE cloud	(0.5, 0.8)	0.75	0.4	150°

This paper has been typeset from a TEX/LATEX file prepared by the author.